Global and Planetary Change 267 (2026) 105690

Contents lists available at ScienceDirect

Global and Planetary Change

journal homepage: www.elsevier.com/locate/gloplacha

Research Article

Astronomical calibration of the Jurassic Hettangian Stage

Ke Zhao [a,b], Stephen P. Hesselbo [b,*], Chunju Huang [c], Clemens V. Ullmann [b,d], Magret Damaschke [e], Teuntje P. Hollaar [b], Mengjie Jiang [f], Melanie J. Leng [e]

[a] Key Laboratory of Exploration Technologies for Oil and Gas Resources, Ministry of Education, College of Resources and Environment, Yangtze University, Wuhan 430100, China
[b] Camborne School of Mines, Department of Earth and Environmental Sciences, University of Exeter, Penryn Campus, Cornwall TR10 9FE, UK
[c] School of Earth Science, China University of Geosciences (Wuhan), Wuhan 430074, China
[d] State Key Laboratory of Geomicrobiology and Environmental Changes, China University of Geosciences (Wuhan), Wuhan 430074, China
[e] British Geological Survey, Keyworth, Nottingham NG12 5GG, UK
[f] Chengdu University, Office of International Cooperation and Exchange, Chengluo Road 2025, 610106, China

ARTICLE INFO

Editor: Dr. Huaichun Wu

Keywords:
Astrochronology
Timescale
Time series analysis
Hettangian duration
Nonlinear process

ABSTRACT

The first stage of the Early Jurassic, the Hettangian, records the aftermath and recovery immediately following the end-Triassic mass extinction. To fully understand the post-extinction Earth processes, an accurate timescale is required. Although several studies have attempted astronomical calibration, results are controversial and differ by a factor of more than two. Here we propose a new age model based on multiple time series datasets (X-ray fluorescence, core gamma ray, magnetic susceptibility, organic carbon isotopes) from the Prees 2C borehole, Cheshire Basin, UK, which provides a more complete Hettangian succession than the classic composite section in the Bristol Channel area. The resulting minimum duration of the Hettangian is 2.18 Myr based on a 405 kyr tuned age model, and we find no compelling evidence for the much longer duration of up to 4 Myr recently proposed, indicating a relatively brief post-extinction recovery time. By anchoring through existing U-Pb dates for the Triassic-Jurassic boundary and incorporating the uncertainties of dating and stratigraphic gaps, the Hettangian is suggested to range from 201.36 ± 0.18 Ma to 199.18 ± 0.18 Ma. The Hettangian timescale established in this study provides an important reference for improving the international geological time scale (GTS) of the Jurassic Period.

1. Introduction

The end-Triassic through Early Jurassic time (~202–175 Ma) was marked by a series of rapid perturbations in climate, environment, and global geochemical cycles, such as occurred at the end-Triassic mass extinction and in its aftermath (Hesselbo et al., 2002; Blackburn et al., 2013; Smith et al., 2014; Hull, 2015; Percival et al., 2017). Astrochronology and establishment of an astronomical timescale (ATS) for the Early Jurassic (Ruhl et al., 2010; Ruhl et al., 2016; Xu et al., 2016) are of particular importance because they lay the foundation for identifying and understanding the key Earth system processes and their rates during and after a major mass extinction event (Hesselbo et al., 2004; Guex et al., 2012; Thibodeau et al., 2016; Atkinson and Wignall, 2019; Singh et al., 2023; Bos et al., 2024).

Research on sedimentary cycles of the Hettangian stage, the first subdivision of Jurassic time, dates back to the 1940s, when possible astronomically-driven deposition of the Blue Lias limestone beds at Lyme Regis, SW England, was first tentatively suggested (Shukri, 1942). The duration of the Hettangian has since been much debated, but hitherto no consensus has been reached. Several researchers have focused on the visible lithological cyclicity and numbers of cycles to attribute astronomical forcing (Weedon, 1986; Waterhouse, 1999; Paul et al., 2008). Using different geological datasets, mostly from the same region in the SW of the United Kingdom, the duration of the Hettangian was estimated as >1.29 Myr (Weedon et al., 1999), >2.86 Myr (Weedon and Jenkyns, 1999), and ~ 1.8 Myr (Ruhl et al., 2010; Hüsing et al., 2014; Xu et al., 2016), with limited constraints available by radioisotopic dating (e.g. ~2 Myr from Schaltegger et al. (2008)). Additionally, other studies indirectly constrain the duration of the Hettangian stage from younger strata through an astronomical timescale anchored in the Toarcian stage (Ruhl et al., 2016; Storm et al., 2020; Hudson et al., 2025).

* Corresponding author.
E-mail address: s.p.hesselbo@exeter.ac.uk (S.P. Hesselbo).

https://doi.org/10.1016/j.gloplacha.2026.105690
Received 23 February 2026; Received in revised form 17 August 2026; Accepted 24 August 2026
Available online 25 August 2026
0921-8181/© 2026 The Authors. Published by Elsevier B.V. This is an open access article under the CC BY license (http://creativecommons.org/licenses/by/4.0/).

A detailed study of the Hettangian was carried out by Weedon et al. (2019), who analysed magnetic susceptibility and ammonite biostratigraphic data from a number of localities including the natural exposures of the Somerset coast (United Kingdom, Fig. 1). Considering local stratigraphic incompleteness, they proposed a ~4.1 Myr duration for the Hettangian, which is approximately double that suggested in most previous studies. Nonetheless, some new floating cyclostratigraphy studies from the Schandelah-1 core of Lower Saxony Basin, Germany (Bos et al., 2024), the Niekłań PIG core of the Polish Basin (Lodowski et al., 2024) and Carnduff-2 core of the Larne Basin, Northern Ireland (Perera et al., 2025) continue to suggest a short Hettangian duration. Multi-section estimates using the TimeOpt approach by Hounslow et al. (2025) also indicated a relatively short earliest Hettangian (Tilmanni Zone and Planorbis Subzone) duration. To test the controversial proposal of a long Hettangian, new analysis is required using high-quality successions lacking long periods of non-deposition or erosion and characterized by multiple high-resolution datasets.

The Prees 2C borehole, drilled in 2020–21 as part of an International Continental Scientific Drilling Program (ICDP) project, recovered an expanded Hettangian marine succession targeted specifically for cyclostratigraphic study and complementary to now much-studied legacy core from the Llanbedr (Mochras Farm) borehole situated ~100 km to the west (Fig. 1). Here, we present an analysis of multiple geochemical and geophysical datasets from the Prees core to cover the entire Hettangian (late Rhaetian to the early Sinemurian) to establish an astronomical timescale including estimates of the lengths of ammonite-based chronozones. At the same time, we consider the evidence for the precise timing of eccentricity minima and maxima through the Hettangian and

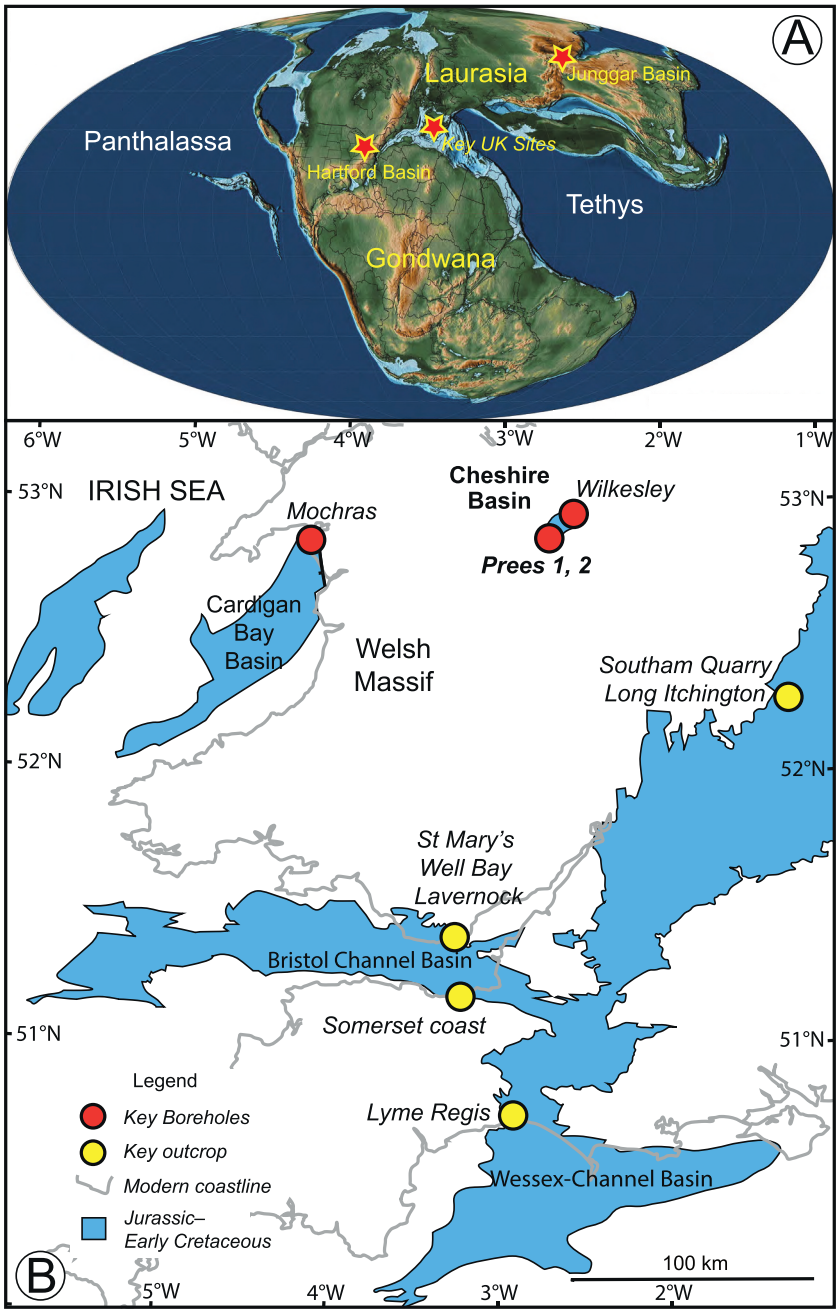


Fig. 1. A: Hettangian paleogeography modified from (Scotese, 2014), and locations of the Hartford Basin (Kent et al., 2017), key UK sites (Storm et al., 2020; Hesselbo et al., 2023), and the Junggar Basin (Sha et al., 2015). B: Occurrence of Jurassic and Early Cretaceous strata in the central and southern UK with locations of boreholes and outcrop sections referred to in this study (adapted from Pharaoh, 1996)).

their sedimentological expression and assess whether the core records the sedimentological effects of a long astronomical obliquity signal.

2. Geological setting

The Prees 2C borehole (Hesselbo et al., 2023) is sited in the Cheshire Basin (Shropshire, England). The Cheshire Basin, active from the Permian through to at least the Early Jurassic, extends geographically from the Manchester area south into Shropshire (Fig. 1). The basin comprises a half-graben with a series of well-defined bounding faults along its eastern and southeastern margins (Evans et al., 1993; Plant et al., 1999), with basin formation primarily controlled by subsidence along the Wem-Red Rock fault system (Evans et al., 1993). The geological succession in the Cheshire Basin includes the Mercia Mudstone Group, the Penarth Group and the Lias Group (Warrington et al., 1999) which collectively span the Triassic-Jurassic transition. The Permian-Triassic fill of the Cheshire Basin is extraordinarily thick, indicative of long and continuous history of extensional movement on the bounding faults (Evans et al., 1993). Subsidence continued into the Early Jurassic based on the proven but mostly unexposed Jurassic Lias Group composed predominantly of calcareous and silty mudstone in the vicinity of Prees (Evans et al., 1993).

The Prees 2C borehole recovered approximately 620 m of latest Triassic to Early Jurassic strata, dating through the Jurassic-Triassic transition and into the early Pliensbachian (Fig. 2A). Ammonite biostratigraphy and organic carbon-isotope stratigraphy provide the detailed relative age framework. The Hettangian stage at Prees spans from 592.33 to 464.86 m (mccd; corrected core depth, see Hesselbo et al. (2023) and Ullmann et al. (2026) for details), with a thickness of 127.47 ± 1.38 m (Fig. 2). Specifically, the depth interval of the Tilmanni (592.33–583.30 m), Planorbis (583.30–555.59 m), Liasicus (555.59–514.04 m), and Angulata (514.04–464.86 m) chronozones and their constituent subzones can be further identified based on ammonite fossils from this core and from the nearby Wilkesley borehole (or using carbon-isotope stratigraphy in the case of the base of the Hettangian) (Hesselbo et al., 2023; Ullmann et al., 2026).

3. Samples and methods

3.1. Geochemical and geophysical data

Detailed descriptions of the analytical methods used to obtain the data evaluated in this study are given in Hesselbo et al. (2023) and Ullmann et al. (2026). Project data include ammonite chrono-biostratigraphy, multi sensor core logging (MSCL – Geotek), carbon isotope ratios of bulk organic matter, and core scanning x-ray fluorescence (XRF – Itrax) (BGS Core Scanning Facility, 2022). The MSCL (magnetic susceptibility and natural gamma ray emission) measurements were carried out at step size of 2 cm, and the XRF data were measured in 1 cm increments. The stable carbon isotope data used herein were obtained at a resolution of 20 cm although the latest Triassic sample spacing is sometimes at lower resolution due to local lack of organic matter (Ullmann et al., 2026).

3.2. Time series analysis

High resolution geochemical and geophysical records were used for time series analysis through the Matlab Acycle software (Li et al., 2019) and Astrochron R package (Meyers, 2014). The analytical steps and parameters are summarized in Table 1.

Detrending can enhance high-frequency signals in the spectrum, but also can suppress low-frequency signals, leading to the loss of some long-

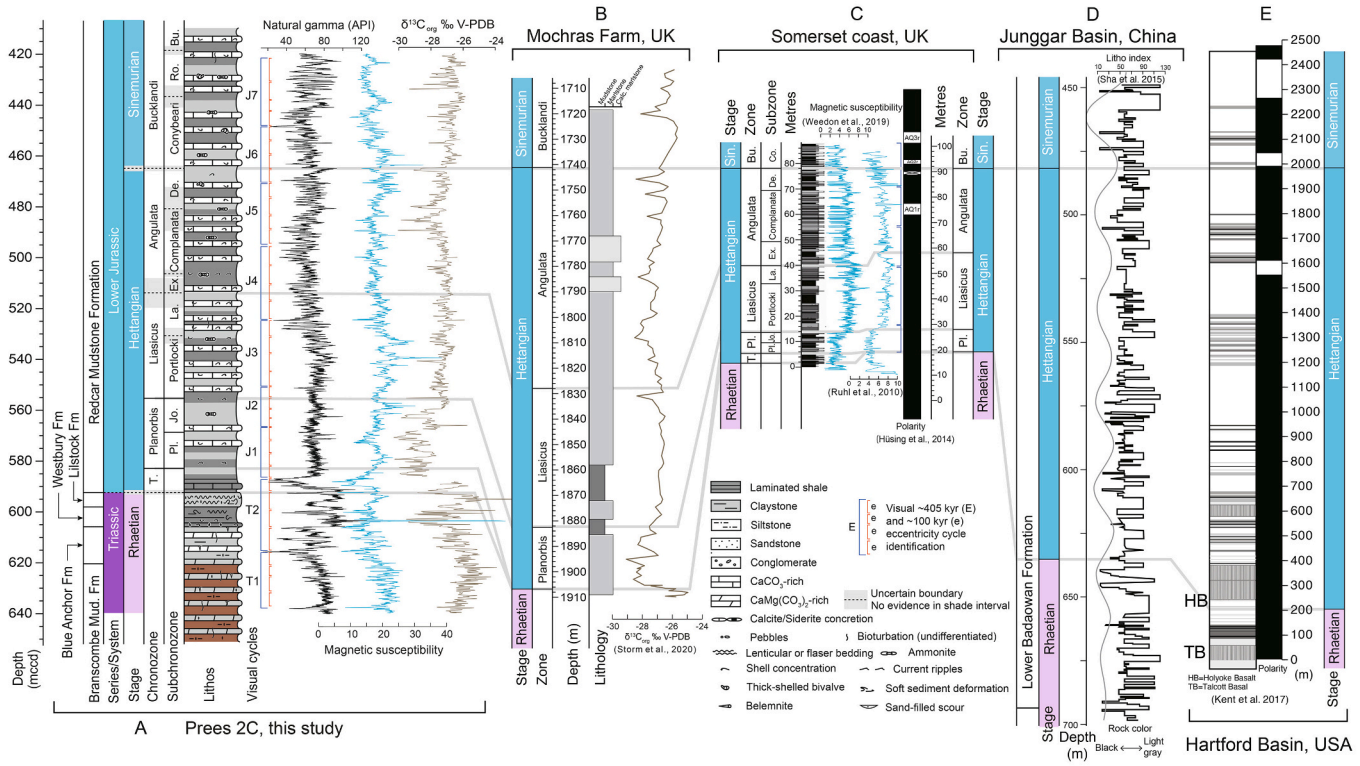


Fig. 2. Overview of lithofacies and key datasets from the Hettangian of boreholes at Prees (A) and Mochras (B), the Somerset coast, UK outcrop (C), Junggar Basin, NW China (D), and Hartford Basin, USA (E). Carbon-isotope record and lithology of Mochras drill core (B) are from Ullmann et al. (2021) and Storm et al. (2020). Magnetic susceptibility data from Somerset coast (C) are from Weedon et al. (2019) and Ruhl et al. (2010), lithofacies from Weedon et al. (2019) (pale marl = grey, dark marl = dark grey, laminated shale = black, limestone bed = white). Litho-index records from Junggar Basin (D) from Sha et al. (2015), with values indicating rock colour (increasing value from black to pale grey) and lithology. Lithofacies and magnetostratigraphy of Hartford Basin are from Kent et al. (2017). Lithological key also applies to Fig. 3

Table 1
Analytical steps and parameters for time series analysis.

	Processes	Methods	Aims	Parameters
1	Remove spikes		Reduce amplitude suppression	<44,000, >435,000 counts (Löwemark et al., 2019) for Fe, <4 for Zr/Rb
	Detrend	rLOESS	Highlight short-period cycles the amplitudes of which are attenuated by long-term variations	Sliding window covering 40% of overall time series length
	Interpolation	Linear	Synthesise stable sampling rate for further steps	Sampling rate of 1 cm for Ca, Fe, Si/Al, Zr/Rb, 2 cm for GR, MS, and 20 cm for C isotope data
	Smooth	Moving Gaussian	Facilitate visual analysis	5-point smoothing
2	Sedimentation rate assessment	COCO and eCOCO (Li et al., 2018), TimeOpt and eTimeOpt (Meyers, 2019)	Estimate the product-moment correlation coefficient between the power spectra of best-guess astronomical solutions and paleoclimate proxy data (Li et al., 2018) to assess the potential sedimentation rate	Sedimentation rate range: 0.1–20 cm/kyr, with a step of 0.1 cm/kyr; Middle age of data: 200 Ma; Sliding window: 55 m, step: 0.74 m; Monte Carlo: 2000 times.
3	Spectral analysis	Multi-taper method	Analyse overall spectrum to identify the likely orbital frequencies	Robust AR(1) red noise modelling (Mann and Lees, 1996) and SWA noise modelling (Weedon et al., 2019)
4	Filter	Gauss bandpass	Filter identified orbital forcing frequency, isolate target astronomical cycle curve	Bandpass of >25% central frequency (Kodama and Hinnov, 2015)
5	Depth-time conversion	Convert the depth scale to time scale (Laskar, 2020) by iteration of steps 3 and 4	Construct age model	Tuning based on 405 kyr cycle minima.

term cycles (e.g., ~1.2 Myr and ~2.4 Myr). The COCO/eCOCO step (Table 1) was processed by comparing the spectra of detrended data and a target spectrum for the earliest Jurassic; thus the results can be affected by the detrending process (Li et al., 2018). The robust AR(1) model may also produce false positive results in the spectral signal, leading to misidentification of astronomical cycles (Smith, 2023). Therefore, an improved smoothing window averaging (SWA) model (Weedon et al., 2019) was applied in the present study to check the confidence level for the tested spectrum. Cycles that were identified visually based on raw data features and described lithofacies were also taken into consideration in the identification of possible astronomical cycles as discussed further below.

4. Cycle analysis of the Hettangian at Prees

4.1. General observations on Hettangian strata at Prees

The total thickness of the marine Hettangian succession at the principal UK localities increases from the Somerset coast (~80 m) through Prees (~130 m) to Mochras (~170 m), and is comparable to fluvio-lacustrine strata in the Junggar Basin, NW China (Fig. 2), where astrochronology has also been applied (Sha et al., 2015). All these successions are far thinner than the continental Hettangian strata (~1800 m) in the Hartford Basin, eastern USA, comprising sedimentary strata together with ~200 m total thickness of Holyoke and Hampden Basalts (Kent and Olsen, 2008; Kent et al., 2017). Noting that the Hartford Basin was an actively subsiding continental *syn*-rift basin in the Early Jurassic, the exceptional thickness should not be used as a straightforward indicator of stage duration.

The ammonite biostratigraphy and carbon-isotope stratigraphy from Prees 2C are consistent with data from the Wilkesley borehole (about 15 km from Prees), Mochras, and the Somerset coastal exposures (Storm et al., 2020; Hesselbo et al., 2023; Ullmann et al., 2026). The base of the Hettangian in Prees 2C, i.e., the Triassic–Jurassic boundary, is at or below a psiloceratid ammonite fragment at depth of 583.27 mccd (Ullmann et al., 2026). Carbon-isotope stratigraphy indicates that the system boundary probably lies at the junction between Lilstock Formation and Redcar Mudstone Formation of the Lias Group (Fig. 2) (Hesselbo et al., 2023). However, there is a small degree of uncertainty due to a lack of age-diagnostic fossils recovered so far from the bottom ~9 m of the Redcar Mudstone Formation at Prees. The Prees 2C core shows relatively thicker chronozones compared to the Somerset coast, especially the basal zone of the Jurassic, the Tilmanni Zone (Fig. 2).

The Hettangian at Prees mainly comprises mudstone and calcareous mudstone (Fig. 2) the latter prominent particularly in the lower Tilmanni Zone where thin beds and laminae of limestone occur within the mudstone (Fig. 2). The lithofacies for the upper Tilmanni, Planorbis, and lowermost Liasicus zones comprises dark grey mudstone with few carbonate-rich beds, whilst the upper Liasicus Zone and all of the Angulata Zone consist of interbedded dark grey mudstone and pale grey bioclast-rich calcareous mudstone or marl (Fig. 3).

The MSCL natural gamma ray logs and selected core-scanning XRF data (Ca-content and Si/Al) are plotted against graphical logs in Fig. 3. Where the GR and Ca curves do not exhibit obvious cyclical changes (i.e., 587–552 m and 469–463 m), the Si/Al elemental ratio can be used as an auxiliary time series for investigation. Si/Al is an established proxy for grain size change, because it mostly reflects the quartz/clay ratio which in turn has a relationship to grain size (Liang et al., 2013). Grain size can alternatively be represented by the Zr/Rb ratio (Bahr et al., 2014; Wu et al., 2020; Sinnesael et al., 2025). Lastly elemental data for Fe are also considered; the mineral hosts of Fe may be more complex than Ca, with the element being present largely in early diagenetic pyrite, but also clay minerals and carbonate phases of diverse origins.

These time series datasets and the accompanying visual core descriptions from Prees show clear lithological cycles ranging from 50 to 150 cm. As is abundantly documented in many studies, such cycles in the Lias Group record alternations in the depositional environment from relatively quiet water, more clay-rich and generally poorly oxygenated bottom water conditions, to relatively oxic, more silty conditions with more biogenic carbonate (Hallam and Lang, 1960; Hesselbo and Jenkyns, 1995; Hesselbo et al., 2004).

4.2. Astronomical cycles in the depth domain

4.2.1. Visual cycle interpretation, Prees 2C

Gamma ray and calcium content records show opposing trends because of dilution of clay by carbonate (Fig. 3). An obvious up-section change within both datasets is apparent at the depth of ~550 mccd, where weak cyclical variation below gives way to a strong high-

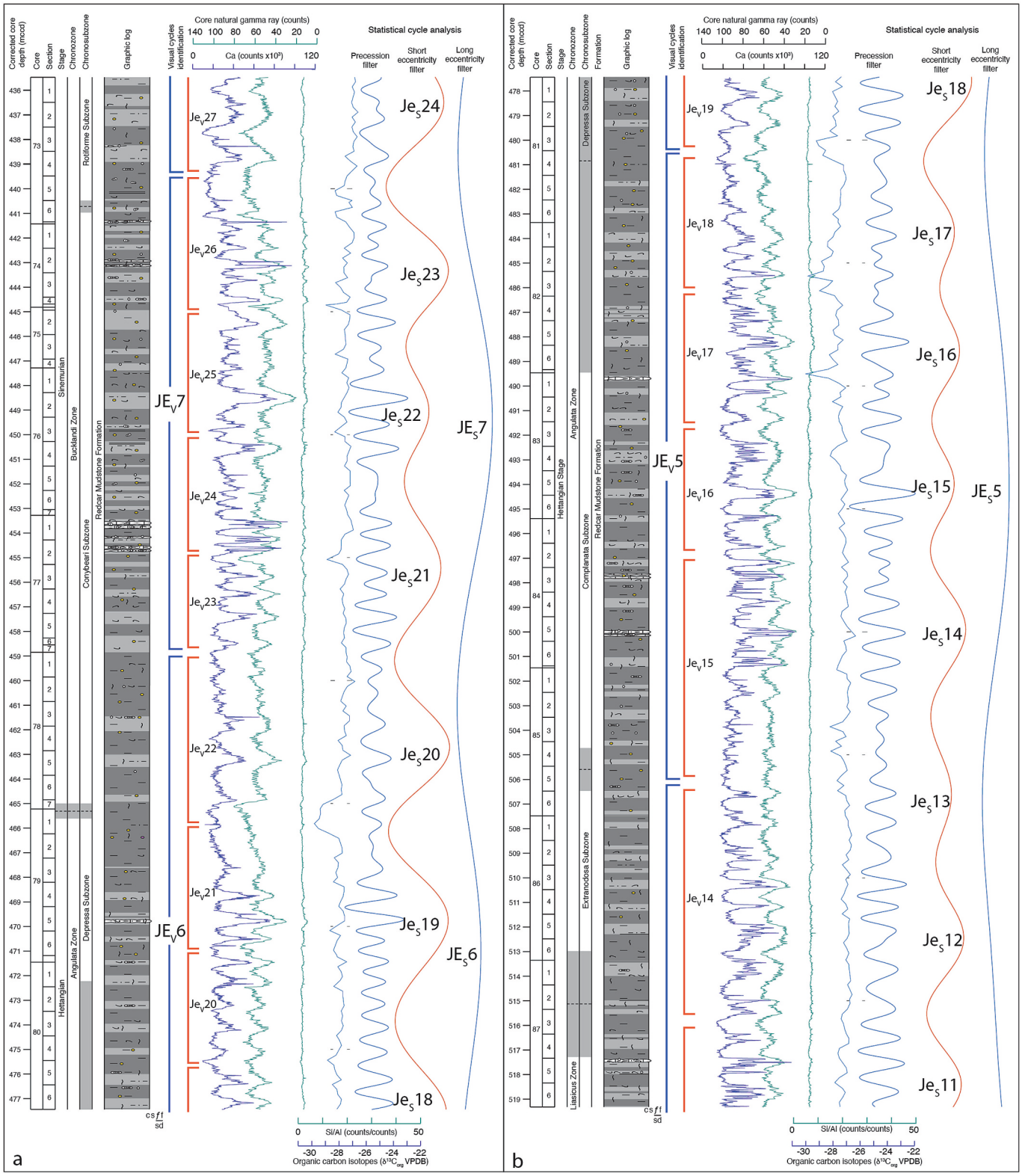


Fig. 3. Detailed lithofacies, visual cycle interpretation, core-scanning data, and cycle filter outputs for the Hettangian Stage, Prees 2C. For clarity, the continuous lithofacies and data records are separated into four panels (a: 477–436 mccd, b: 519–478 mccd, c: 561–520 mccd, d: 604–562 mccd). The curves in each panel from left to right are – Ca content, core natural gamma ray, Si/Al value, precession filter, short eccentricity filter, long orbital eccentricity filter, and organic carbon isotopes. The colour of the curve is consistent with its labels. Identified cycles are labelled as follows: JE_v - Jurassic visual long Eccentricity, TE_v - Triassic visual long Eccentricity, JE_s - Jurassic statistical long Eccentricity. Je_s - Jurassic statistical short eccentricity. For key to graphic logs refer to Fig. 2.

frequency cyclical variation through to the top of the Hettangian (Figs. 2 and 3). The elemental Fe record shows a similar trend to GR, except

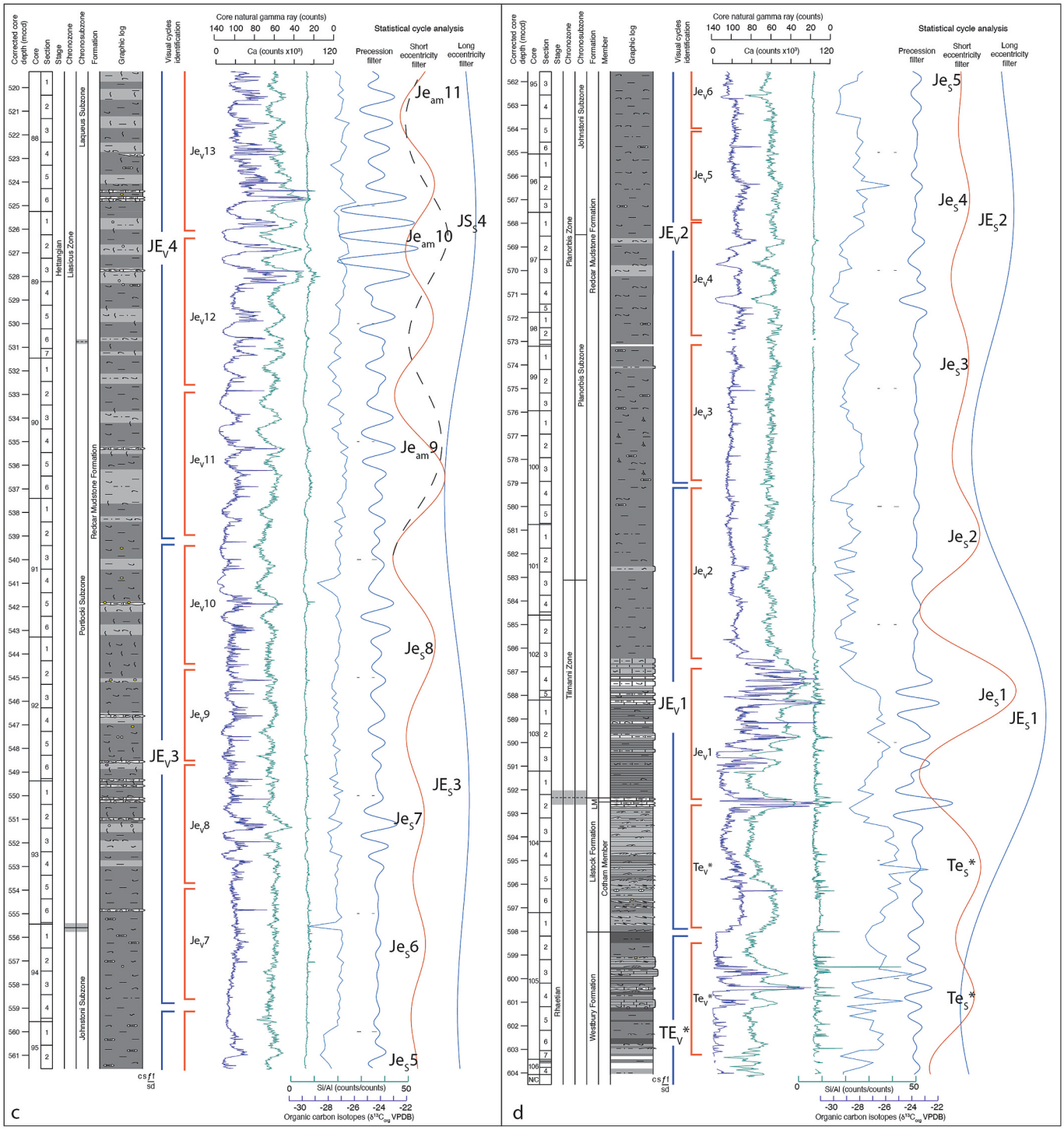


Fig. 3. (*continued*).

when the Fe signal is dominated by the presence of pyrite identified by visual core observation and sulfur readings from XRF (see Section 4.2.2). Also, the elemental Fe content does not show the strongly developed high-frequency small-scale core GR cycles of the later Hettangian succession. The MS and C-isotope results, in contrast to the core GR, Ca and Fe records, mainly show relatively long-term cycles, with no obvious high-frequency periodicity (Fig. S1A, B).

From visual inspection, the visual long-eccentricity cycles (JE_V) were selected based on: 1) the obvious precession to short-eccentricity relationship in raw data; 2) consistent cycles expressed in multiple records, and; 3) the amplitude of precession consistent with the modulation of eccentricity cycle. According to the criteria of visual cycle selection, ~1.4 m cycles are found in the raw GR and Ca data series, especially the interval from 550 to 420 mccd, with a greater thickness of ~1.5 m through ~540–510 mccd and reduced thickness of ~1 m evident around ~510–470 mccd (Fig. 3b). A relatively thicker cycle composed of a bundle of five ~1.4 m cycles is also observed, and the 1:5 ratio indicates that these small-scale cycles likely correspond to astronomical precession (Fig. 3). Therefore, if identification of the precession cycle is correct, the long eccentricity cycle would be expected to be ~28 m thick and the strata to have an average sedimentation rate of ~7 cm/kyr. It is also notable that amplitude variations in visually identified precession

cycles correspond closely to candidate eccentricity cycles, as expected from theory and observation in this depositional setting (e.g., Hollaar et al., 2023), and allowing hypothetical recognition of maximum eccentricity (high amplitude precession) and minimum eccentricity (low amplitude precession). Visually identified long-eccentricity cycles are marked by JE_v in the present study (Fig. 3). In the depth interval of 640–550 mccd, a relatively weak and high frequency cyclicity is visible in the GR and Ca datasets (~0.8 m period), suggesting a likely lower sedimentation rate in the deeper part of the core. In the studied interval a total of 9 long eccentricity cycles are thus recognized by visual analysis (Fig. 2). The interpreted long-eccentricity cycles are labelled T_v* and JE_v1–JE_v8 in Fig. 3.

We note that there appears to be an additional short eccentricity cycle in JE_v4 (i.e., five cycles) indicated in Fig. 3 which we discuss further in Section 4.2.2. Anomalies in constituent short-eccentricity cycles are also found in JE_v1, manifesting as a rapid change in GR values near the base of the Hettangian. On this evidence we interpret that there is either a hiatus or condensation at ~592.5 mccd (Fig. 3d). This possible hiatus at the Triassic–Jurassic boundary is supported, albeit weakly, by sedimentological evidence: there is an abrupt upward change in depositional environment from very shallow water of the Cotham Member, through a very thin (18 cm) Langport Member representing marine muddy carbonate deposition, into the millimeter-laminated mudstone of the basal Lias (Warrington, 1997; Hesselbo et al., 2023).

4.2.2. *Statistical cycle identification and comparisons with visually identified cycles, Prees 2C*

According to the correlation coefficient results (see Section 3.2), the average sedimentation rate for Prees is 7.8 cm/kyr with a confidence level of over 90% (H_0 significance level < 0.1) resulting from 2000 Monte Carlo simulations comparing the correlation between target periodogram (spectrum of La2010d solution (Laskar et al., 2011)) and studied datasets (Fig. 4). TimeOpt analysis of the GR, Ca, and Fe records suggest ~7 cm/kyr, ~10.5 cm/kyr and ~16 cm/kyr sedimentation rate in the spectral domain (periodogram vs. astronomical frequencies) and time domain (short eccentricity envelope vs. long eccentricity filter) (Fig. 5). The ~16 cm/kyr value differs significantly from the visually observed cycles, and if correct implies precession cycles of more than 3 m thickness alongside a long eccentricity cycle of ~64 m and a Hettangian duration of less than 1 Myr; such inference is strongly at odds with visual observations on the core as well as any previous cycle and radioisotopic analysis and so is rejected here. The eCOCO results of core GR, Ca and Fe data series (Fig. 4) show similar trends as the TimeOpt analysis, with low sedimentation rate at the bottom (~7 cm/kyr), increasing above ~560 mccd (complex and unstable, ~11 cm/kyr), and then decreasing above ~480 m (~8 cm/kyr). The same changes of sedimentation rate can also be inferred from the thickness variations of visually identified precession cycles in GR and Ca curves, where there are thicker cycles in the middle segment. By integrating the COCO/TimeOpt method and the visual cycle identification, we consider ~7–8 cm/kyr as the most likely sedimentation rate for Prees 2C during the Hettangian Stage.

From the overall multi-taper method (MTM) spectral analysis results (Fig. 6), GR, Ca and Fe content datasets have similar properties with power concentrated at ~27, 10, 7, 4.7, 3.2, 2.6, 1.7, 1.3, and 1 m. Therefore, based on results from COCO and TimeOpt analysis, the peaks at ~27, ~7, ~3, and ~1.3 m, with an approximate ratio of 20:5:2:1, are hypothesized to represent the astronomical cycles of long and short eccentricity, obliquity, and precession. Based on the SWA noise model, the ~27 and ~10 m peaks from GR, Ca and Fe datasets pass the 1% false discovery rate (FDR) criterion and the ~6.7, ~4.9, 2.6, ~1.6, ~1.4, ~1, ~0.7, ~0.59, ~0.56, and ~0.39 m peaks reach the 95% chi-square level (Fig. S2). The ~27, ~6.7, ~2.6, and ~1.4 m peaks using this age model

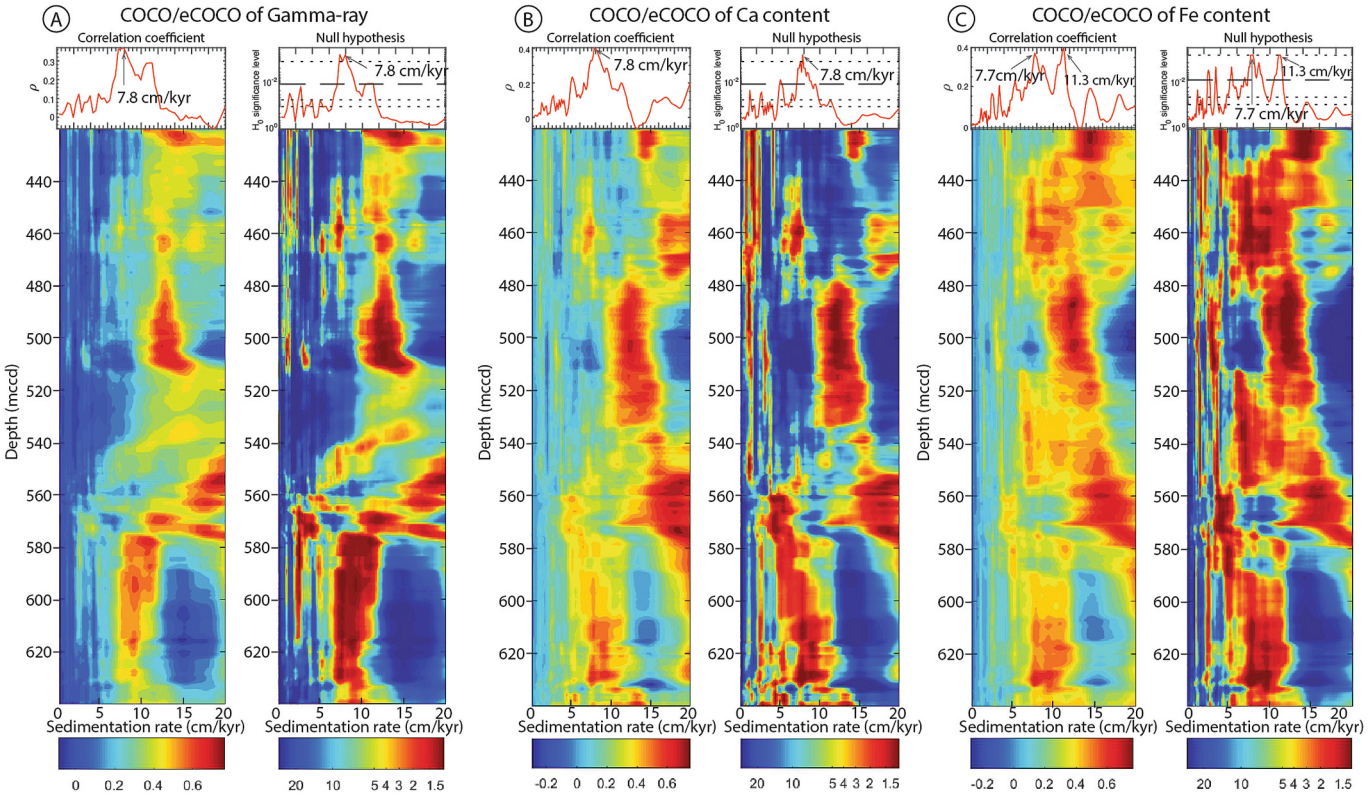


Fig. 4. COCO and eCOCO results of Prees gamma-ray, Ca and Fe content. The correlation coefficient analysis was processed with 2000 Monte Carlo simulations using the target astronomical spectrum Laskar2010d with middle age of 200 Ma, and the test sedimentation rate range from 0.1 to 20 cm/kyr and a step of 0.1 cm/kyr. eCOCO was preceded with a 55 m sliding window and 0.74 m step.

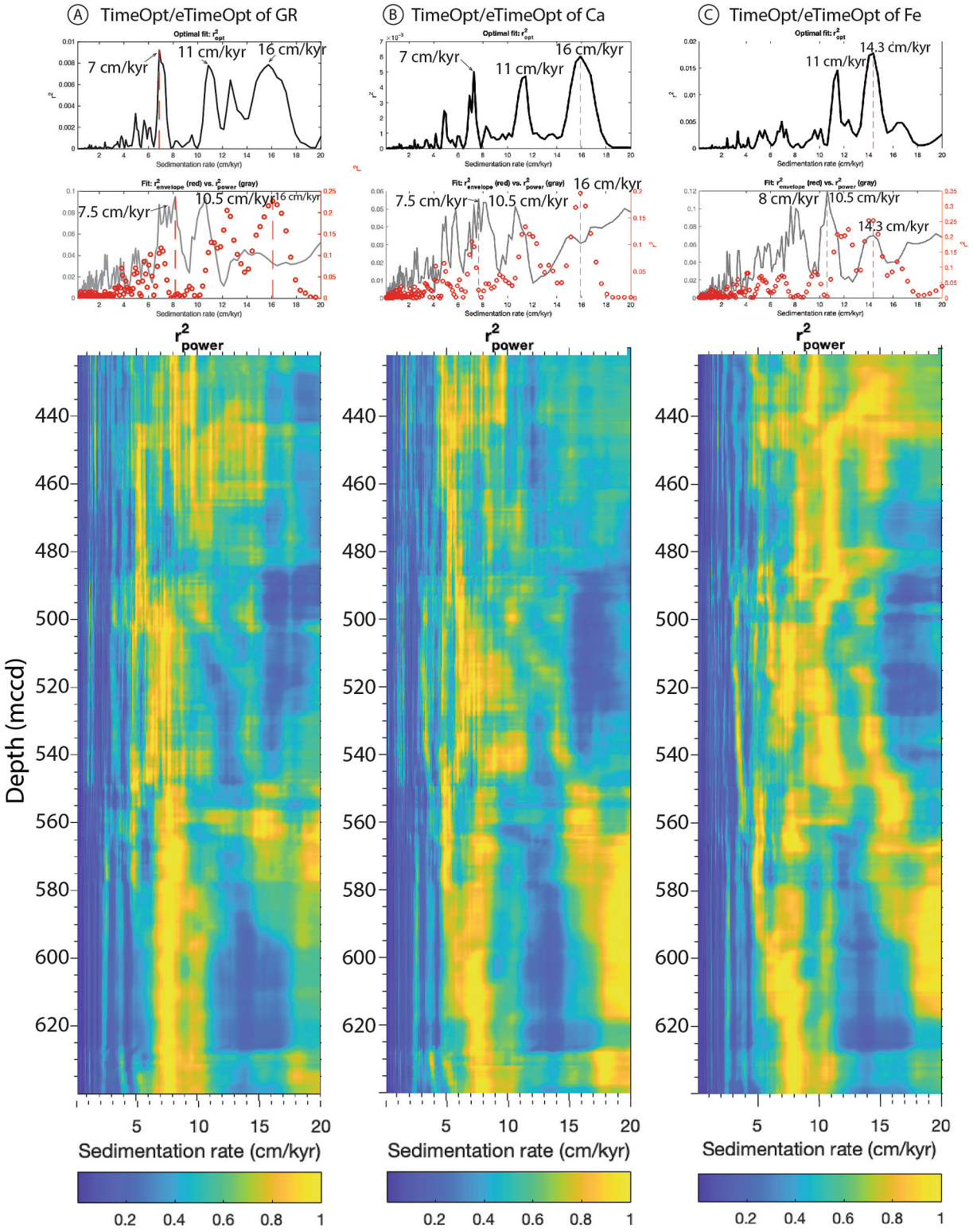


Fig. 5. eTimeOpt results of Prees GR (A), Ca (B), and Fe (C). The analysed data series were detrended using a robust LOWESS (locally weighted scatterplot smoothing) with a smoothing window covering 40% of the data points. Tested sedimentation rate was 0.1–20 cm/kyr, with a linear distribution of 200 test sedimentation rates. The target frequency used the astronomical spectrum Laskar2010d with middle age of 200 Ma. eTimeOpt analysis was performed using a window of 77 m and step of 0.7 m, with the Pearson correlation method.

have an approximate ratio of 20:5:2:1, and are also consistent with the MTM, COCO/TimeOpt and visual cycles, further indicating long and short eccentricity, obliquity, and precession cycles.

Using these hypothesized eccentricity frequencies, the peaks of ~27 m and ~7 m wavelength are filtered using the Gaussian band-pass filter method with the bandwidth covering the entire peak that is broadened by thickness variation caused by varied sedimentation rate (GR: 0.01637–0.05819, 0.1000–0.1872; Ca: 0.01637–0.05818, 0.105–0.185;

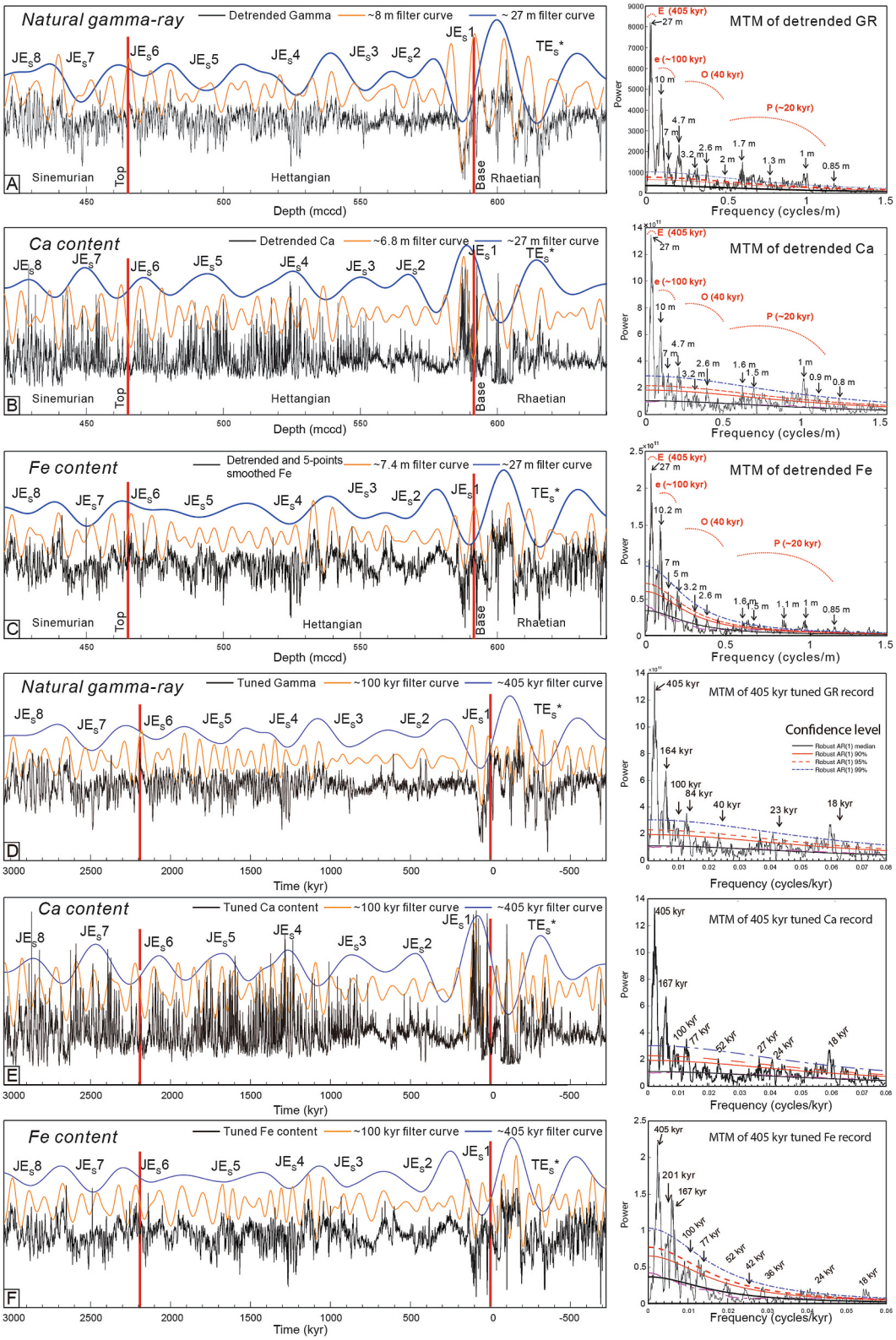


Fig. 6. Cycle analysis of time-series datasets of GR, Ca and Fe in the depth domain (A-C) and time domain (D-F). The detrended data are shown in left side panels alongside the interpreted 405 and 100 kyr eccentricity cycle filters, and related MTM spectra of detrended data records are in the right-side panels. All raw data are detrended by 40% thickness using LOESS method (A-C), and the Fe record is further processed by 5-point smoothing to eliminate abnormal peaks (C). D-F are the 405-kyr tuned results of A-C, respectively, with related MTM spectra shown in right side panels. The bandpass filter widths in the depth domain are as follows: GR: 0.01637–0.05819 m^{-1}, 0.1000–0.1872 m^{-1}; Ca: 0.01637–0.05818 m^{-1}, 0.105–0.185 m^{-1}; Fe: 0.02336–0.04936 m^{-1}, 0.106–0.180 m^{-1}. All filters of the tuned data apply a bandpass of 0.001469–0.003469 cycles/kyr for ~405 kyr cycle and 0.007–0.013 cycles/kyr for ~100 kyr cycle. Confidence levels of MTM analysis are all derived using robust AR(1) red noise model (Mann and Lees, 1996). (For interpretation of the references to colour in this figure legend, the reader is referred to the web version of this article.)

Fe: 0.02336–0.04936, 0.106–0.180). A total of 9.5 × ~27 m cycles are filtered (labelled TE_s* and JE_s 1–8), representing the ~405 kyr astronomical cycle. From the filter result (Figs. 3, 6) cycles JE_s 4–5 have a greater thickness than others, in agreement with the results of eCOCO and visual inspection (Fig. 3).

Analyses of the MS and C-isotope data are not fully consistent with the results described above. Peaks of 23, 17.2, 9.5, 5.2, 3.3, 2.5, 1.6, and 1.1 m are found from of detrended MS data, and the identification of long eccentricity signal of ~27 m (based on the MTM of core GR, Ca, and Fe records) is mixed with a strong ~17.2 m cycle signal. Therefore, the mixed long eccentricity cycle spectrum leads to a different filter output, where the TE_s*–JE_s4 cycles are similar to the core GR, Ca, and Fe filter output, whereas JE_s5–8 do not show a clear long eccentricity cycle for these time series (Fig. S1A). The carbon-isotope time series shows an MTM spectral result with the main peaks of 29.7, 17.2, 10.2, 7, 5.9, 3.5, and ~1.3 m. The peak of ~29.7 m, corresponding to the previous result of ~27 m, and the peak ratios for ~29.7, 7, 2.7, and 1.3 m of 20:5:2:1, indicate potential astronomical cycle signals. The filter centred on 29.7 m shows that cycles JE_s3–7 roughly correspond to the GR, Ca, and Fe filter output, while cycles JE_s1–2 do not show a good filter result (Fig. S1B). Raw C-isotope data show relatively stable values through 555–420 mccd depth, and larger amplitudes of change in the 600–555 mccd range (Fig. 2A), which may explain the weak cycle identification of JE_s1 and JE_s2 in particular. Carbon-isotope records of the Hettangian, especially around the Triassic–Jurassic transition where the mass extinction event occurred, are likely directly and indirectly affected by non-cyclic factors such as volcanic forcing, resultant climatic changes, water mass anoxia, and associated carbon-cycle tipping points (Fujisaki et al., 2018; Korte et al., 2019; Hesselbo et al., 2020a; Ullmann et al., 2026).

The anomalous number of short eccentricity cycles comprising JE4, whether recognized visually or expressed in the bandpass filer requires further comment. It is particularly noteworthy that this is the only part of the core record where the recognized short eccentricity cycles no longer correspond to amplitude modulation of precession (Fig. 3c). The carbonate layers at ~524 mccd cause a higher Ca count and larger amplitude of the Ca record, which will further affect the statistical eccentricity cycle identification. Therefore, we treat the amplitude modulation in this interval as more convincing indicator of short eccentricity than either a crude cycle count or gaussian filter would suggest, but have to leave open the possibility that an undetected hiatus may be present in which 3 short eccentricity cycles are missed.

Overall, the astronomical timescale derived from core GR, Ca and Fe records shows consistent results, which can be used to construct the detailed age model for Prees (Fig. 6D-F). Both visually and statistically recognized cycles are taken into consideration. The age model developed here was first generated using Acycle software based on the core depth position of the minimum of each statistically derived 405-kyr cycle. Considering the atypical development of carbonate layers in JE_s4, the minimum position is adjusted based on the visually recognized JE_v4. Through building the age model based on the long eccentricity cycles (Table S1) and tuning the dataset to the time domain, an astronomical timescale covering about ~3.8 Myr, including a Hettangian of ~2.2 Myr duration, is established for the latest Triassic and early part of the Early Jurassic analysed here (Fig. 6D-F).

All analysed data show an obvious peak compatible with the ~405 kyr cycle in the MTM spectral results except for the MS time series (Fig. S1C). Equally, all datasets show a strong ~170 kyr spectral signal which may correspond to the ~173 kyr orbital obliquity (Boulila et al., 2018). We discuss the origin of this latter cycle in more depth in Section 7 below.

5. Previous studies on the duration of Hettangian

5.1. Debates of Hettangian duration in different sites

Several studies have estimated the duration of the Hettangian using different outcrops and boreholes, of which the St Audrie's Bay to Quantoxhead composite section ('Somerset coast') is most intensively studied and thought to have global correlation potential for the Hettangian stage (Ruhl et al., 2010; Hüsing et al., 2014; Xu et al., 2016; Weedon et al., 2019). Most previous studies of these outcrops have yielded a similar duration of ~1.8 Myr for the Hettangian by establishing an astronomical age model, for example the ~1.8 Myr duration of the ATS from lithofacies, organic C-isotopes, and Total Organic Carbon (TOC) (Ruhl et al., 2010), the ~1.7 Myr duration by counting the inferred ~100 kyr eccentricity cycles of organic C-isotopes combined with a paleomagnetic investigation (Hüsing et al., 2014), and ~1.89 Myr duration from organic carbon-isotope cyclostratigraphic analysis (Xu et al., 2016). This latter result is shorter than that from Storm et al. (2020) based on the Mochras borehole dataset (but still within the uncertainties), which indicates a residual duration of ~2.3 ± 0.5 Myr for the Hettangian Stage based on the estimated durations of other stages of the Early Jurassic (Table 2), and is consistent with the Geomagnetic Polarity Time Scale (GPTS) in the Hartford Basin, USA (Kent and Olsen, 2008; Kent et al., 2017; Kent et al., 2018).

It should be noted that some of the differences between duration estimates stem from different concepts for the definition of the base of the Hettangian, the Global Stratotype Section and Point (GSSP) which was established in 2010 (Hillebrandt et al., 2013). For example Ruhl et al. (2010), predating this decision, take the base of the Jurassic as equivalent to the base of the Planorbis Zone, and so their duration does not include the Tilmanni Zone (which in their interpretation has a duration of 100 kyr), resulting in a shorter Hettangian estimate. Similarly, Storm et al. do not compensate for missing time in the Sinemurian at Mochras due to faulting (see Hudson et al., 2025), which conversely forces a longer duration for the preceding Hettangian stage. Recent studies on the Sinemurian Stage by Leu et al. (2024) suggested a minimum ~6.2 Myr duration using low-resolution (downhole) gamma ray data of the Prees 2C core, and this duration was updated to ~7.3 Myr by Hudson et al. (2025) through analysis of the calcium and organic carbon isotope data from Mochras. The longer Sinemurian stage necessitates a short duration (~2 Myr) for the Hettangian stage using an U-Pb CA-ID-TIMS radioisotopic anchor point in the early Toarcian and given that cyclostratigraphic calibration for the Pliensbachian is well documented and reasonably stable (Hudson et al., 2025).

In contrast, Weedon et al. (2017) described several substantial hiatuses in the Hettangian strata of the Somerset coast based on field observations and from cross plots of biostratigraphic and cycle correlation, which they argued were not fully accounted for in previous studies. For the Somerset coast, using their methodology, prominent hiatuses are located at the base of the Planorbis Subzone and the base of the Johnstoni Subzone (both Planorbis Zone), and in the Depressa Subzone of the Angulata Zone, amongst other levels (Weedon et al., 2017). Considering these hiatuses, Weedon et al. (2019) carried out an analysis of the cyclicity within a composite of the magnetic susceptibility datasets of the Somerset coast section together with Southam Quarry (Long Itchington, Warwickshire, England), Lavernock (South Wales coast), and Lyme Regis (Devon/Dorset, SW England) — see Fig. 1 for map —, and proposed a >4.1 Myr duration for the Hettangian Stage, including an estimated ~0.89 Myr for the total duration of hiatuses. Nevertheless, the long duration of the Hettangian is largely a consequence of the ~2 Myr length estimate for the Tilmanni and Planorbis zones combined, with a ~0.7 m thickness of the short eccentricity cycle in Somerset, 0.81 m in Wales, and 0.46 m in Dorset. However, the identification of the eccentricity cycle in these two basal zones may be compromised by the thinness of segments selected by Weedon et al. (1.5–13.5 m, fig. 5 in Weedon et al. (2019)) and also the method of spectral analysis (Smith, 2023). These thin segments would make it hard to confidently identify a signal of a relatively thick eccentricity cycle if it existed in the spectrum using either a robust AR1 model (Mann and Lees, 1996) or improved smoothed window averaging (SWA) model (Weedon et al., 2019). The restricted length of targeted data segments would also

Table 2
Boundaries of zones and subzones of Prees in depth and time.

Stage	Zone	Subzone		Depth (mccd)	ATS Time (kyr)	Base Boundary		Zone Duration (kyr)
						Depth (mccd)	ATS Time (kyr)	
Sinemurian	Bucklandi	Conybeari	base	465.00	2193	465.31	2187 ± 42	/
Hettangian	Angulata	Depressa	top	465.61	2181			~780 ± 70
Hettangian	Angulata	Depressa	base	472.23	2059	480.85	1910 ± 160	
Hettangian	Angulata	Complanata	top	489.47	1757			
Hettangian	Angulata	Complanata	base	504.72	1538	505.59	1527 ± 41	
Hettangian	Angulata	Extranodosa	top	506.45	1516			
Hettangian	Angulata	Extranodosa	base	512.98	1431	515.13	1403 ± 54	
Hettangian	Liasicus	Laqueus	top	517.28	1375			~660 ± 90
Hettangian	Liasicus	Laqueus	base	530.67	1184	530.77	1183 ± 48	
Hettangian	Liasicus	Portlocki	top	530.86	1181			
Hettangian	Liasicus	Portlocki	base	555.41	743	555.59	739 ± 76	
Hettangian	Planorbis	Johnstoni	top	555.76	735			~580 ± 80
Hettangian	Planorbis	Johnstoni	base	568.53	440	568.43	442 ± 51	
Hettangian	Planorbis	Planorbis	top	568.32	444			
Hettangian	Planorbis	Planorbis	base	583.10	164	583.12	163 ± 22	
Hettangian	Tilmanni	/	top	583.14	163			~160 ± 20
Hettangian	Tilmanni	/	base	592.33	0	592.33	0	

*The mccd depth of zone and subzone are based on Ullmann et al. (2026). Boundary-age uncertainties combine the biostratigraphic placement uncertainty with the cyclostratigraphic model spread generated by the alternative visual, filtered and amplitude-modulation tie-point schemes (Table S1), using root-sum-of-squares. They do not include unquantified missing time caused by a possible hiatus or an incorrectly counted 405-kyr cycle. Durations of zones are rounded to the nearest 10 kyr to avoid unjustified precision.

complicate identification of orbital cycles through the ratios between lengths of cycles.

5.2. Re-appraisal of MS-based cyclostratigraphy for the Somerset sections

To further assess the results obtained by (Weedon et al., 2019) and compare with the new results from Prees, we re-analysed the published magnetic susceptibility data of the Somerset coast sections to explore the sedimentation rates. Application of the eCOCO method suggests a change in sedimentation rate from ~3.4 cm/kyr or >8 cm/kyr in the 1.5 m (base Hettangian) to 20 m height interval, rising to ~6 cm/kyr in the ~20–55 m interval, and then decreasing to ~2.8 cm/kyr from 55 m to the top of the section (Fig. 8). Similar rate changes are evident in the Fast Fourier Transform evolutionary spectral analysis (based on the FFT-MTM package in Acycle software), especially the hypothetical short eccentricity frequency values of ~0.33 m^{-1} (0–25 m), ~0.15 m^{-1} (25–45 m), ~0.2 m^{-1} (45–55 m), and ~ 0.4 m^{-1} (55–87.5 m) (Fig. 7).

Compared to the spectra of the four separate stratigraphic 'segments'

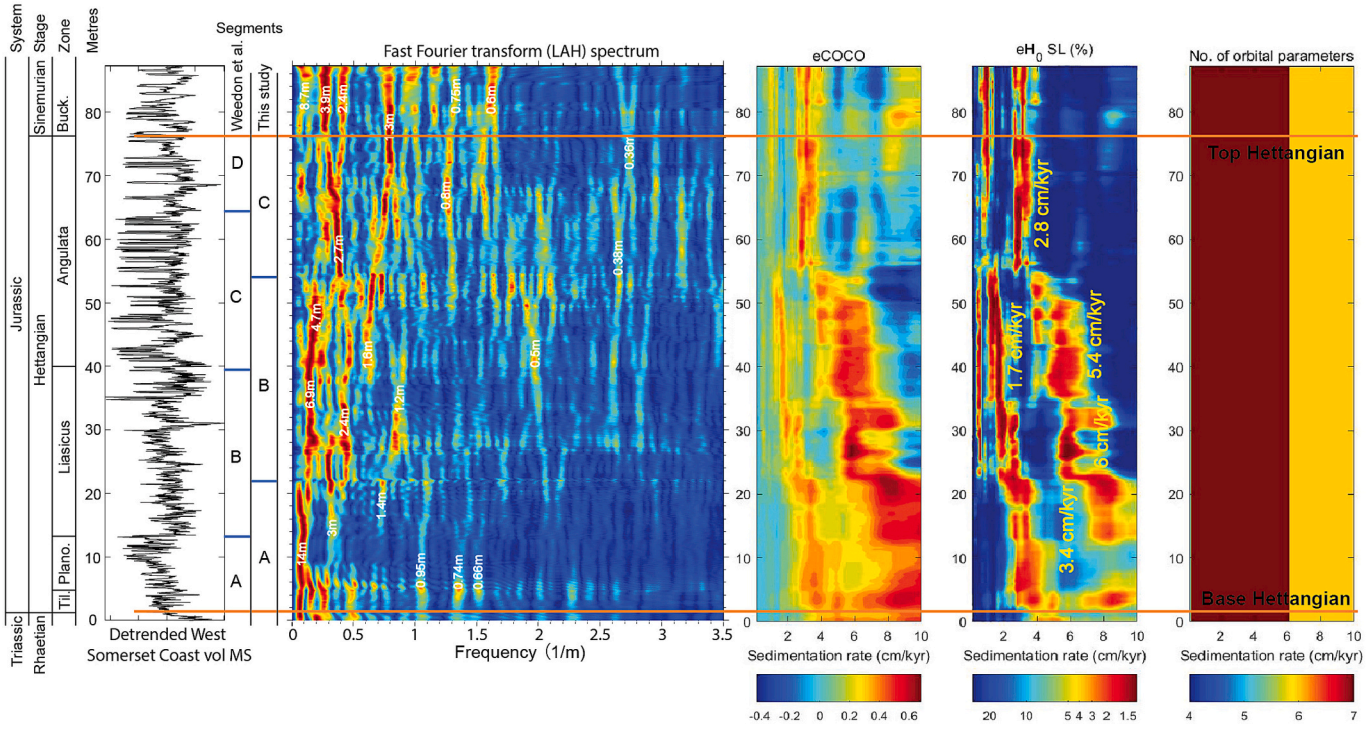


Fig. 7. FFT-MTM (left panel) and eCOCO (right panel) analysis of magnetic susceptbility record of the St Audrie's Bay/East Quantoxhead composite section. FFT-MTM evolutionary spectral analysis of magnetic susceptibility record from the St Audrie's Bay/East Quantoxhead composite section. The tested frequency is ranged from 0 to 3.5 m^{-1}, and the window is 17.448 m, step is 0.13958 m. The test sedimentation rate range from 0.1 to 20 cm/kyr with a step of 0.1 cm/kyr. The Laskar2010d solution is selected as target model and the middle age is 200 Ma. 2000 Monte Carlo simulation tests have been processed with a sliding window of 22.08 size and 0.3 m step.

from Weedon et al. (2019), which roughly correspond to the four intervals listed above, the evolutionary spectrum partly supports their segments B and D but disagrees strongly in the lowest segment A. The spectrum of segment A of Weedon et al. (2019) may thus be interpreted differently, potentially resolving the conflict of the apparent anomalously long duration of the Tilmanni and Planorbis zones. Based on the changing sedimentation rate from eCOCO analysis and the evolutionary spectrum, a new segment subdivision is proposed here, comprising segment 1 (0–22 m), segment 2 (22–55 m), and segment 3 (55–87.5 m). The boundaries of segment B and C and segment C and D from Weedon et al. (2019) do not show any obvious step changes in sedimentation rate, but instead rather continuous change. According to the evolutionary spectrum and correlation coefficient, a total of 22 short eccentricity cycles can be filtered in the present study spanning the latest Rhaetian to earliest Sinemurian, which is consistent with visually identified short eccentricity cycles and the filter output of Weedon et al. in the Liasicus and Angulata zones (Fig. S3). The duration of the Somerset coast composite section is thus calculated (~19 short eccentricity cycles, Fig. S5) as ~1.87 Myr without hiatuses (Table 2), which is consistent with previous results for a short Hettangian (Ruhl et al., 2010;

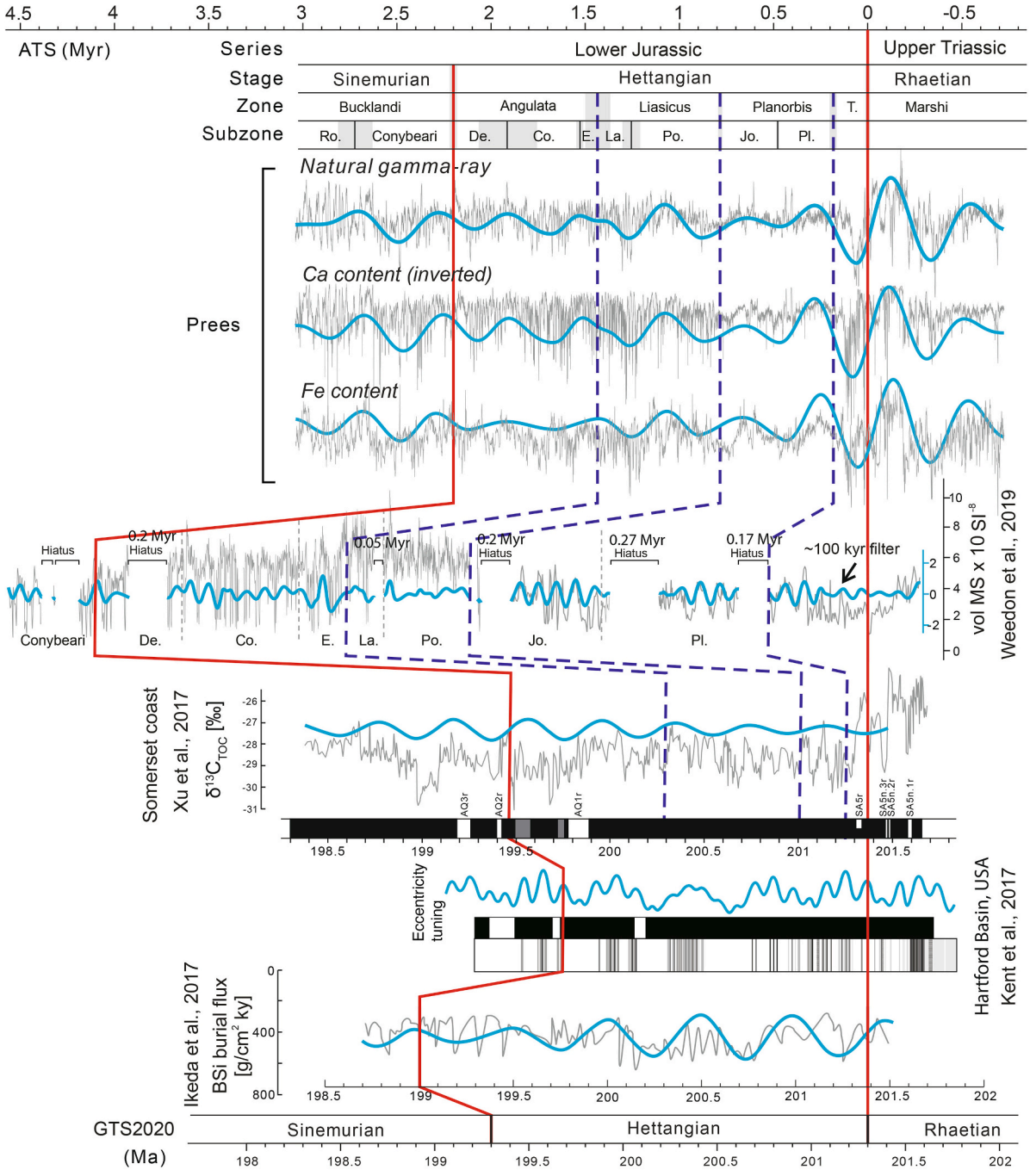


Fig. 8. Comparison of astronomical timescales between Prees and previous studies from Somerset Coast, UK (Weedon et al., 2019; Xu et al., 2016), Hartford Basin, USA (Kent et al., 2017), Inuyama, Japan (Ikeda et al., 2017), and GTS2020 (Hesselbo et al., 2020b). Vertical red lines show the base and top of the Hettangian, and blue dashed lines represent ammonite zone boundaries. The light grey data records together with blue curves are the tuned data and their 405 kyr filter in time domain, except for that from Weedon et al. (2019), which is the ~100 kyr filter. (For interpretation of the references to colour in this figure legend, the reader is referred to the web version of this article.)

Hüsing et al., 2014; Xu et al., 2016).

To further explore this result, the Lavernock and Lyme Regis sections were also re-analysed in the present study (Fig. S4) using the data of Weedon et al. (2019). The evolutive spectrum of the Lyme Regis section shows strong peaks at ~4.4, ~1.56, ~0.7, 0.46, ~0.26, and ~0.17 in the Planorbis and Tilmanni zones, with a reasonable astronomical cycle ratio of 20:5:2:1. The 0.46 m signal, which was interpreted as a short-eccentricity cycle signal by Weedon et al. (2019), could thus instead correspond to obliquity (with a sedimentation rate of ~1.15 cm/kyr).

The evolutive spectral analysis of the Lavernock section shows signal peaks of ~3, ~0.8, ~0.4, ~0.34, ~0.29, ~0.2, ~0.17, and ~0.15 m (Fig. S4). This result is roughly consistent with Weedon et al. (2019), which has a strong and continuous ~0.8 m signal throughout the dataset, with several ~2.8–4.2 m low frequency signals at 0–12 m height in the section. It may be assumed that the 0.8 m cycle represents short eccentricity, and the ~3.2 m cycle corresponding to long eccentricity cycle (with a 1:4 ratio) as concluded by Weedon et al. (2019). However, due to the thinner and incomplete strata at Lavernock, it may also be challenging to identify a much longer cycle if it existed. Therefore, it is also plausible that the ~3 m cycle at Lavernock represents short eccentricity (with a sedimentation rate of ~3 cm/kyr).

Regarding the placement and magnitude of hiatuses from Weedon et al. (2017), assuming that, as proposed here, the Planorbis Zone from Lavernock and Lyme Regis sections also had a relatively rapid sedimentation rate, the duration of hiatuses of 0.64 Myr within the Planorbis Zone (Fig. 8) should also be compressed to ~0.16 Myr. Therefore, the total duration of the Hettangian from the Somerset Coast composite section is increased to ~2.28 Myr, comprising ~1.87 Myr of deposited strata, 0.16 Myr of hiatus in the Planorbis Zone, and 0.25 Myr of hiatus in the Liasicus (0.05 Myr) and Angulata (0.2 Myr) zones (Table 3, Fig. 8). We further stress that the 'Somerset coast' is a composite section and there is also potential error involved in splicing the sections together because there is lateral variation in the diagenetic cementation of limestone beds used for correlating one section to another (Whittaker and Green, 1983). This source of error is at present underexplored.

6. Astronomical timescale for the Hettangian from Prees 2C

According to our new age model, the Hettangian stage is estimated to have the duration of 2.18 Myr (Fig. 8), which is well within the uncertainty of the duration from GTS2020 (201.4 ± 0.2 Ma to 199.5 ± 0.3 Ma; (Hesselbo et al., 2020b). Specifically, the duration of four ammonite chronozones within the Hettangian – Tilmanni, Planorbis, Liasicus, and Angulata – are 0.16 Myr, 0.58 Myr, 0.66 Myr, and 0.78 Myr, respectively, assuming that zonal boundaries are located at the mid-point of biostratigraphic uncertainty (Table 2). Direct radio-isotopic dating is currently missing for the Prees core, and is not soon likely to yield precise dates due to the lack of volcanic ash beds (although refined Re-Os dating is a distinct future possibility). Therefore, the geochronological age of the Triassic-Jurassic boundary (201.36 ± 0.17 Ma, (Wotzlaw et al., 2014)) and Hettangian-Sinemurian boundary (199.43 ± 0.10 Ma; (Schaltegger et al., 2008), (Guex et al., 2012)) from the marine Pucara Group in Peru can be referenced here for the chronostratigraphic calibration. Of these two possible tie points the age of the Triassic-Jurassic boundary is much preferable, because the Hettangian-Sinemurian boundary radioisotopic age is relatively more imprecise (a larger gap between biostratigraphic indicators) and in a succession that is difficult to correlate to NW Europe (e.g., see Hudson et al., 2025). Hence, we propose the Hettangian stage be assigned an age range from of 201.36 to 199.18 Ma plus uncertainty on the tie point age.

The uncertainties on the duration and calibrated age should be considered in several aspects. Firstly, the radioisotopic uncertainties of the U-Pb date of the Triassic-Jurassic boundary by EARTHTIME tracers amount to 0.17 Myr (Wotzlaw et al., 2014; Hesselbo et al., 2020b). With the advancement of radioisotopic dating methodology, estimates of the age of boundaries and events are now increasingly hampered by (bio-) stratigraphic limitations (Hesselbo et al., 2020b). Specifically, there exists a ~ 5.6 m ammonite fossil gap between the first occurrence of *Psiloceras spelae spelae* and the last occurrence of *Choristoceras crickmayi* (fig. 1B in Schoene et al. (2010), where the true first evolutionary occurrence of *P. spelae* could be at any position in this gap. The duration of the ~5.6 m ammonite fossil gap can be calculated according to the dated age of samples LM4-100/101, LM4-90, and LM4-86 (Wotzlaw et al., 2014; Hesselbo et al., 2020b). Assuming the sedimentation rate of the fossil gap remains unchanged, the average sedimentation rate can be calculated as 4.31 cm/kyr, and the duration of the ~5.6 m ammonite fossil gap is ~130 kyr, corresponding to an uncertainty of ±65 kyr.

A further substantial uncertainty arises from cycle identification, filter selection, the placement of 405-kyr tuning tie points and interpolation between adjacent tie points. The positional uncertainty is defined as the maximum absolute deviation from the adopted tie point using the three methods considered (visual cycles; statistical cycles; amplitude modulation cycles; Table S1). The maximum difference of the cyclostratigraphic model uncertainty could be therefore calculated, which may further affect the ages and durations of individual zones and subzones with generally no change for the total duration. The total calculated cyclostratigraphic uncertainty is combined with biostratigraphic boundary uncertainty by Root Sum of Squares (RSS) method reported in Table 2. Hinnov (2018) suggested that high-quality intercalibration between astrochronology and radioisotope geochronology may achieve an absolute-age uncertainty of approximately 0.05%, equivalent to approximately 0.10 Myr at the Triassic–Jurassic transition. We therefore regard ±0.10 Myr as a conservative minimum uncertainty for absolute astrochronological ages, although this value is not treated as an additional independent component of the interval-duration uncertainty.

Uncertainty of the Hettangian duration also may come from the potential for hiatuses in the Prees 2C borehole itself, although we have

Table 3
Duration of biozones according to the astronomical timescale.

Zone and subzone		Prees		Somerset Coast, Bristol Channel Basin					Mochras Farm	Hartford Basin
		Prees 2C		Reanalysed (Weedon et al., 2019)	(Weedon et al., 2019)		(Xu et al., 2016)	(Ruhl et al., 2010)	(Hüsing et al., 2014)	(Storm et al., 2020)	(Kent and Olsen, 2008)
An.	De.	0.29	0.78	0.88 (1.08)	0.46	1.34	0.82	0.8	0.82	/	/
	Co.	0.39			0.62						
	Ex.	0.1			0.26						
Li.	La.	0.22	0.66	0.66 (0.71)	0.19	0.66	0.72	0.75	0.66	/	/
	Po.	0.44			0.46						
Pl.	Jo.	0.30	0.58	0.22 (0.38)	0.69	1.59	0.24	0.25	0.22	/	/
	Pl.	0.28			0.89						
Ti.		0.16	0.16	0.11	0.52		0.11	/	/	/	/
Sum		~2.18		~1.87 (2.28)	4.1		1.89	1.8	1.7	2.3 ± 0.5	1.69

*All data are presented in Myr. Values in bracket of reanalysed MS record volume are the durations including hiatuses. An. – Angulata, Li. – Liasicus, Pl. – Planorbis, Ti. – Tilmanni, De. – Depressa, Co. – Complanata, La. – Laqueus, Po. – Portlocki, Jo. – Johnstoni.

not found clear evidence so far to prove the existence of any hiatuses. The unmatched cycle hierarchy of short and long eccentricity in JE_s4 is compensated by interpretation of amplitude modulation of precession cycles instead, and the age model is established according to long eccentricity, therefore having no influence on the estimated Hettangian duration.

The total uncertainty of the base Hettangian age (±0.18 Myr) was propagated using the RSS method, combining the analytical uncertainty from CA-ID-TIMS dating (Wotzlaw et al., 2014) and the stratigraphic uncertainty derived from the biostratigraphic gap (Fig. S5). Using that logic the base Hettangian age of 201.36 ± 0.18 Ma and Hettangian duration of at least 2.18 Myr can be estimated. Separately, the Hettangian-Sinemurian boundary age, resulting in the combined uncertainties of 0.18 Myr of base Hettangian and propagated cyclostratigraphic uncertainty of ~0.04 Myr, would be 199.18 ± 0.18 Ma.

Compared to previous published durations of the Hettangian from other records, the result of this study is similar with that of Storm et al. (2020) from the Mochras drill core, but longer than all the previous durations for the Somerset coast except Weedon et al. (2019), or for the Hartford Basin (Kent et al., 2017) (Table 3). The magnetostratigraphic analysis from the Hartford Basin (Kent and Olsen, 2008) and Somerset coast (Hüsing et al., 2014) both show three short reversed polarity zones, and these have been used to help define the chronostratigraphy in the Hartford Basin leading to roughly similar stage durations. The astronomical tuning of Somerset and the Hartford Basin sections was also used to define the top of the Hettangian in the Junggar Basin of China (Sha et al., 2015). The results from a multi-section applying the TimeOpt sedimentation rate analysis across the Triassic-Jurassic boundary indicated a duration of 262 ± 53 kyr for the Tilmanni Chronozone and 238 ± 27 kyr for the Planorbis Subchronozone, yielding a combined duration of approximately 0.50 Myr (Hounslow et al., 2025), broadly comparable to the ~0.44 Myr obtained from the Prees-2C core although they assigned a longer Tilmanni Zone.

As discussed above, the greatest contrast in estimated durations between Weedon et al. (2019) and the present study are for the Planorbis and Tilmanni zones. This is also reflected by the slope changes in the duration cross plot between Prees and the Somerset coast section (Fig. 9). The here reanalysed Somerset MS record of Weedon et al. (2019) shows shorter Tilmanni and Planorbis zones, roughly the same duration of Liasicus, and a longer Angulata Zone compared to that from Prees (Table 3), although the total Hettangian duration of both are fairly consistent (2.18 Myr from Prees and 2.28 Myr from Somerset coast). Specifically, the reanalysed MS results shows that the Tilmanni Zone is 0.05 Myr shorter in Somerset than that in Prees, but it is still comparable considering the biozone uncertainties and the potentially incomplete strata at the base Hettangian on the Somerset coast. Hiatuses in the Planorbis Zone may also cause a 0.2 Myr shorter duration in Somerset compared to Prees. The duration of the Liasicus Zone is consistent for both Prees and the Somerset coast, and the 0.03 Myr difference is well within the uncertainties. The duration of the Angulata Zone on the Somerset coast is 0.3 Myr longer than that in Prees, indicating a potential hiatus may exist in the Angulata Zone of Prees, or that there is an error in construction of the composite Somerset section. Notably the composite Somerset section is spliced in the lower Angulata Zone based only on correlation of limestone marker beds with the inherent uncertainty that this entails.

7. Climatic effects of the astronomical cycles in Prees and expression of the long obliquity cycle

The classical Milankovitch (e.g. 405, 100, ~40, ~20 kyr) and other, generally longer, astronomical cycles (e.g. 2.4 Myr, 1.2 Myr, 173 kyr) are all involved in regulating the Earth's climate. The ~173 kyr periodicity is associated with the interaction between the nodal precession frequencies of Earth and Saturn ($s_3 - s_6$) and is expressed as a periodicity of Earth's orbital inclination and an amplitude-modulation cycle of Earth's obliquity (Hinnov, 2000, 2018). Owing to the large mass of Saturn, the $s_3 - s_6$ is unusually stable and may therefore serve as a useful astronomical metronome in stratigraphic successions characterized by dominant obliquity forcing and low precession contribution (Boulila et al., 2018; Hinnov, 2018). This astronomical cycle and its climate effects are well expressed in the Prees borehole.

Here we find that the long obliquity cycle and the long and short eccentricity cycles of Prees show a mutually inhibitory relationship,

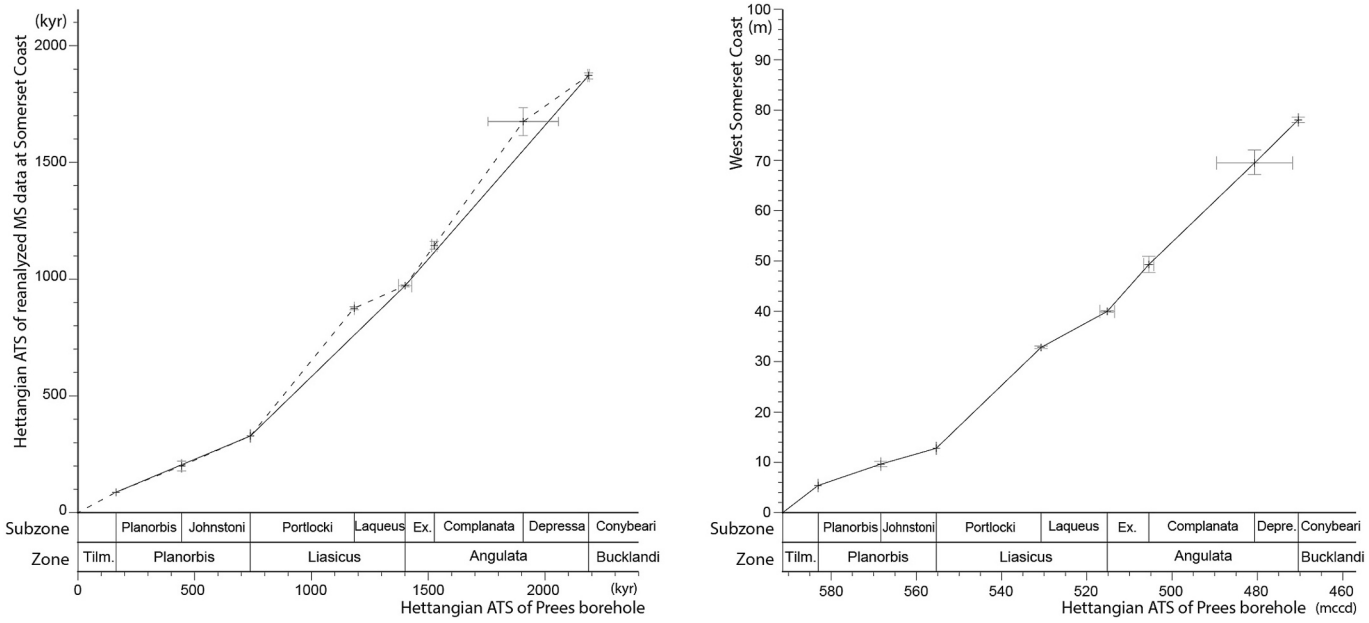


Fig. 9. Crossplots of Hettangian duration between Prees borehole and reanalysed Somerset Coast section in time domain (a) and depth domain (b). Symbols represent corresponding ammonite chronozone and subchronozone boundaries. Horizontal error bars show boundary-placement uncertainty in the Prees 2C core according to Ullmann et al. (2026), and vertical error bars show the corresponding uncertainty in the Somerset composite section (Weedon et al., 2019). The solid and dashed line in (a) connects successive correlated zone and subzone boundaries, respectively. Changes in slope illustrate differences in relative minimum durations of different zones.

both in the raw depth series (Fig. 3) and the evolutive spectrum (Fig. S6). Through depth intervals ~510–~470 mccd (corresponding to JE_s5 and JE_s6), the long obliquity signal of ~12 m in the evolutive spectrum is enhanced while the eccentricity signal is weak (Fig. S6). This feature can also be identified in the raw data records for the long eccentricity cycles JE_v5 and JE_v6, where an obvious intermediate cycle comprises two short eccentricity cycles (Fig. 3a, b). The phenomenon of eccentricity cycle concealment has also been found in the marine sediments of southern China for the early Triassic, with multiple concealments of the 405 kyr cycle along with enhancement of the obliquity cycle signal (Li et al., 2016). It is noted, however, also that well-documented long obliquity cycles are rare in raw data (Huang et al., 2021). This observation leads us to hypothesise that nonlinear processes (the threshold effects) of the Earth's climate system are occurring in JE_s5 and JE_s6; that is, a series of nonlinear processes and multiple equilibria could amplify the small amplitude changes of obliquity and ultimately have manifested in the paleoclimate proxies (Huybers, 2006). Previous studies have shown that the processes in the mid- and low-latitude regions of the climate system can respond nonlinearly to solar radiation forcing, which may be related to the global carbon cycle (Westerhold et al., 2018; Westerhold et al., 2020; Ao et al., 2021). Huang et al. (2021) also proposed the threshold model to explain the influence of a ~173 kyr long obliquity cycle on Earth's climate system and organic carbon burial.

In the present study, the transition between eccentricity cycle and long obliquity cycle indicates the change of dominant astronomical cycle pacing of the Hettangian climate. The long obliquity (173 kyr) cycle appears to have regulated the strength of the obliquity forcing by regulating the tilt angle. A possible mechanism proposed by Li et al. (2016) with regard to the Early Triassic, is that the obliquity modulation cycle drives the distribution of global water vapor, resulting in a long-term imbalance between rainfall and evaporation-runoff within the continents, and causing changes in the capacity of continental groundwater reservoirs. The influence of groundwater change may then also be found in global sea-level change, paleoclimate, and the carbon cycle (Huang et al., 2021; Tian et al., 2022).

This transition in dominant climatic pacemakers—from eccentricity to long obliquity—and the associated nonlinear responses highlight a potential complex, astronomically forced climatic backdrop for the Hettangian, which may also have contributed to previously widely ranging estimates for the stage length. The high-resolution astrochronological framework established here allows these climatic oscillations to be precisely dated, providing a temporal template against which the rates of post-extinction biotic recovery can be measured.

Besides astronomical age models, constraints on the pacing of ecosystem recovery in the Early Jurassic derive from radiometric age dates (Schaltegger et al., 2008; Guex et al., 2012; Blackburn et al., 2013). Such radiometric ages have been of outstanding importance for the construction of the geologic timescale (Hesselbo et al., 2020b) and establishment of synchroneity of CAMP volcanism with the end Triassic extinction and some of the broader patterns of recovery (Blackburn et al., 2013; Thibodeau et al., 2016). However, these ages derive from outcrops with incompletely known relation to European biozonation schemes, in particular the ammonite biozones and subzones which often act as subdivisions to study biotic changes (e.g., (Hallam, 1997)). To study recovery rates at a finer scale, cyclostratigraphic control on the durations of ammonite biozones and reconciliation of contrasting duration estimates for key successions are therefore essential. The data from the Cheshire Basin allows additional tie points to be added to the chronology of biotic recovery via biozone and biosubzone durations of the Hettangian stage, which saw the radiation of Jurassic ammonoids from the genus *Psiloceras* (Page, 2008; Guex et al., 2012) and benthic recovery (Atkinson and Wignall, 2019). The new findings give further weight to a relatively brief Hettangian Stage (~2.18 Myr), and cast doubt on protracted recovery implied by long Tilmanni and Planorbis zones (Weedon et al., 2019), instead arguing for comparatively rapid diversification of biota in the aftermath of the extinction.

8. Conclusions

The timescale of Early Jurassic Hettangian stage is important for understanding the post-extinction processes and improving the international geological timescale of the Jurassic Period. In this study, multiple geochemical and geophysical datasets from the Prees 2C borehole (Cheshire Basin, UK) were used to carry out an astrochronological analysis for the Hettangian stage. The principal findings are:

1. A minimum ~2.18 Myr long duration is established using a 405 kyr cycle tuned age model for the Hettangian Stage in Prees 2C based on cyclostratigraphic analysis, and the age range of the Hettangian is further proposed to be 201.36 ± 0.18 Ma to 199.18 ± 0.18 Ma based on the published U-Pb age of the base of the Hettangian.
2. The magnetic susceptibility data from a previous study on the Somerset coast, Weedon et al. (2019), are re-analysed here. We determine a ~1.87 Myr astronomical duration without hiatuses (2.28 Myr with hiatuses) based on the ~100 kyr eccentricity tuning result, which is consistent with other previous results from the Somerset coast outcrop. The entire duration of 2.28 Myr is also very similar to the present study based on Prees, while some unresolved inconsistencies remain when comparing durations of ammonite biozones.
3. During the Hettangian, a mutually inhibitory relationship is hypothesized between the long obliquity (~173 kyr) and eccentricity cycles. This transition in climatic pacemakers suggests that nonlinear threshold responses amplified obliquity forcing, dominating the climatic changes when eccentricity signals were weak.

CRediT authorship contribution statement

Ke Zhao: Writing – review & editing, Writing – original draft, Visualization, Software, Methodology, Investigation, Formal analysis. **Stephen P. Hesselbo:** Writing – review & editing, Visualization, Supervision, Project administration, Conceptualization. **Chunju Huang:** Writing – review & editing, Supervision, Funding acquisition. **Clemens V. Ullmann:** Writing – review & editing, Supervision. **Magret Damaschke:** Resources, Data curation. **Teuntje P. Hollaar:** Data curation. **Mengjie Jiang:** Data curation. **Melanie J. Leng:** Data curation.

Declaration of competing interest

The authors declare that they have no known competing financial interests or personal relationships that could have appeared to influence the work reported in this paper.

Acknowledgement

Funding for the Early Jurassic Earth System and Timescale Project (JET) was provided by the International Continental Scientific Drilling Program (ICDP, Project 5065), and the UK Natural Environment Research Council (NE/N018508/1). We acknowledge support by National Natural Science Foundation of China (No. 42502129, No. 42230208, No. 42172039, No. 42072137), and the Postdoctoral Fellowship Program of CPSF under Grant GZB20250108. ML and MD publish with the approval of the Director, BGS (NERC).

Appendix A. Supplementary data

Supplementary data to this article can be found online at https://doi.org/10.1016/j.gloplacha.2026.105690.

Data availability

The authors confirm that all data necessary for supporting the scientific findings of this paper have been provided.

References

Ao, H., Liebrand, D., Dekkers, M.J., Zhang, P., Song, Y., Liu, Q., Jonell, T.N., Sun, Q., Li, X., Li, X., Qiang, X., An, Z., 2021. Eccentricity-paced monsoon variability on the northeastern Tibetan Plateau in the Late Oligocene high CO_2 world. Sci. Adv. 7, eabk2318.

Atkinson, J.W., Wignall, P.B., 2019. How quick was marine recovery after the end-Triassic mass extinction and what role did anoxia play? Palaeogeogr. Palaeoclimatol. Palaeoecol. 528, 99–119.

Bahr, A., Jiménez-Espejo, F.J., Kolasinac, N., Grunert, P., Hernández-Molina, F.J., Röhl, U., Voelker, A.H.L., Escutia, C., Stow, D.A.V., Hodell, D., Alvarez-Zarikian, C. A., 2014. Deciphering bottom current velocity and paleoclimate signals from contourite deposits in the Gulf of Cádiz during the last 140 kyr: an inorganic geochemical approach. Geochem. Geophys. Geosyst. 15, 3145–3160.

BGS Core Scanning Facility, 2022. Prees-2C Core Scanning Dataset. NERC EDS National Geoscience Data Centre Dataset. https://doi.org/10.5285/91392f09-25d4-454c-aece-56bde0dbf3ba.

Blackburn, T.J., Olsen, P.E., Bowring, S.A., McLean, N.M., Kent, D.V., Puffer, J., McHone, G., Rasbury, E.T., Et-Touhami, M., 2013. Zircon U-Pb geochronology links the end-Triassic extinction with the Central Atlantic Magmatic Province. Science 340, 941–945.

Bos, R., Zheng, W., Lindström, S., Sanei, H., Waajen, I., Fendley, I.M., Mather, T.A., Wang, Y., Rohovec, J., Navrátil, T., Sluijs, A., van de Schootbrugge, B., 2024. Climate-forced Hg-remobilization associated with fern mutagenesis in the aftermath of the end-Triassic extinction. Nat. Commun. 15, 3596.

Boulila, S., Vahlenkamp, M., De Vleeschouwer, D., Laskar, J., Yamamoto, Y., Pälike, H., Kirtland Turner, S., Sexton, P.F., Westerhold, T., Röhl, U., 2018. Towards a robust and consistent middle Eocene astronomical timescale. Earth Planet. Sci. Lett. 486, 94–107.

Evans, D.J., Rees, J.G., Holloway, S., 1993. The Permian to Jurassic stratigraphy and structural evolution of the central Cheshire Basin. J. Geol. Soc. Lond. 150, 857–870.

Fujisaki, W., Matsui, Y., Asanuma, H., Sawaki, Y., Suzuki, K., Maruyama, S., 2018. Global perturbations of carbon cycle during the Triassic–Jurassic transition recorded in the mid-Panthalassa. Earth Planet. Sci. Lett. 500, 105–116.

Guex, J., Schoene, B., Bartolini, A., Spangenberg, J., Schaltegger, U., O'Dogherty, L., Taylor, D., Bucher, H., Atudorei, V., 2012. Geochronological constraints on post-extinction recovery of the ammonoids and carbon cycle perturbations during the Early Jurassic. Palaeogeogr. Palaeoclimatol. Palaeoecol. 346-347, 1–11.

Hallam, A., 1997. Recovery of the marine fauna in Europe after the end-Triassic and Early Toarcian mass Extinctions. Geol. Soc. Lond. Spec. Publ. 102, 231–236.

Hallam, A., Lang, W.D., 1960. A sedimentary and faunal study of the Blue Lias of Dorset and Glamorgan. Philos. Trans. R. Soc. Lond. Ser. B Biol. Sci. 242, 1–44.

Hesselbo, S., Jenkyns, H., 1995. A comparison of the Hettangian to Bajocian successions of Dorset and Yorkshire. In: Field Geology of the British Jurassic, pp. 105–150.

Hesselbo, S.P., Robinson, S.A., Surlyk, F., Piasecki, S., 2002. Terrestrial and marine extinction at the Triassic-Jurassic boundary synchronized with major carbon-cycle perturbation: a link to initiation of massive volcanism? Geology 30.

Hesselbo, S.P., Robinson, S.A., Surlyk, F., 2004. Sea-level change and facies development across potential Triassic–Jurassic boundary horizons, SW Britain. J. Geol. Soc. Lond. 161, 365–379.

Hesselbo, S.P., Korte, C., Ullmann, C.V., Ebbesen, A.L., 2020a. Carbon and oxygen isotope records from the southern Eurasian Seaway following the Triassic-Jurassic boundary: parallel long-term enhanced carbon burial and seawater warming. Earth Sci. Rev. 203, 103131.

Hesselbo, S.P., Ogg, J.G., Ruhl, M., Hinnov, L.A., Huang, C.J., Ogg, James G., Gabi, M., 2020b. The Jurassic Period. In: Gradstein, Felix, Schmitz, Mark D. (Eds.), Geologic Time Scale 2020, pp. 955–1021.

Hesselbo, S.P., Al Suwaidi, A., Baker, S.J., Ballabio, G., Belcher, C.M., Bond, A., Boomer, I., Bos, R., Bjerrum, C.J., Bogus, K., Boyle, R., Browning, J.V., Butcher, A.R., Condon, D.J., Copestake, P., Daines, S., Dalby, C., Damaschke, M., Damborenea, S.E., Deconinck, J.-F., Dickson, A.J., Fendley, I.M., Fox, C.P., Fraguas, A., Frieling, J., Gibson, T.A., He, T., Hickey, K., Hinnov, L.A., Hollaar, T.P., Huang, C, Hudson, A.J. L., Jenkyns, H.C., Idiz, E., Jiang, M., Johnson, Ben, Krijgsman, W., Korte, C., Leng, M. J., Lenton, T.M., Leu, K., Little, CT.S., MacNiocall, C., Mancenido, M.O., Mather, T. A., Mattioli, E., Miller, K.G., Newton, R.J., Page, K.N., Palfy, J., Pienkowski, G., Porter, R.J., Poulton, S.W., Riccardi, A.C., Riding, J.B., Roper, A., Ruhl, M., Silva, R. L., Storm, M.S., Suan, G., Szucs, D., Thibault, N., Uchman, A., Stanley, J.N., Ullmann, C.V., van de Schootbrugge, B., Vickers, M.L., Wadad, S., Whiteside, J.H., Wignall, P.B., Wonik, T., Xu, W., Zeeden, C., Zhao, K., 2023. Initial results of coring at Prees, Cheshire Basin, UK (ICDP JET Project); towards an integrated stratigraphy, timescale, and Earth system understanding for the Early Jurassic. Sci. Drill. 32, 1–25.

Hillebrandt, A.v., Krystyn, L., Kürschner, W.M., Bonis, N.R., Ruhl, M., Richoz, S., Schobben, M.A.N., Urlichs, M., Bown, P.R., Kment, K., McRoberts, C.A., Simms, M., Tomäsových, A., 2013. The Global Stratotype Sections and Point (GSSP) for the base of the Jurassic System at Kuhjoch (Karwendel Mountains, Northern Calcareous Alps, Tyrol, Austria). Episodes 36, 162–198.

Hinnov, L.A., 2000. New perspectives on orbitally forced stratigraphy. Annu. Rev. Earth Planet. Sci. 28, 419–475.

Hinnov, L.A., 2018. Chapter one - cyclostratigraphy and astrochronology in 2018. In: Montenari, M. (Ed.), Stratigraphy & Timescales. Academic Press, pp. 1–80.

Hollaar, T.P., Hesselbo, S.P., Deconinck, J.-F., Damaschke, M., Ullmann, C.V., Jiang, M., Belcher, C.M., 2023. Environmental changes during the onset of the Late Pliensbachian Event (Early Jurassic) in the Cardigan Bay Basin, Wales. Clim. Past 19, 979–997.

Hounslow, M.W., Posen, P.E., Warrington, G., Page, K.N., 2025. Omission and pacing of events at the Norian–Rhaetian and Triassic–Jurassic transitions in Britain. Geol. Mag. 162.

Huang, H., Gao, Y., Ma, C., Jones, M.M., Zeeden, C., Ibarra, D.E., Wu, H., Wang, C., 2021. Organic carbon burial is paced by a ~173-ka obliquity cycle in the middle to high latitudes. Sci. Adv. 7.

Hudson, A.J.L., Hesselbo, S.P., Hinnov, L.A., Littler, K., Page, K.N., Riding, J.B., Ruhl, M., Ullmann, C.V., 2025. Astrochronology of the Sinemurian Stage from the Llanbedr (Mochras Farm) Core, NW Wales: implications for the Early Jurassic timescale. Vol. Jurass. XXIII, 43–64.

Hull, P., 2015. Life in the aftermath of mass extinctions. Curr. Biol. 25, R941–R952.

Hüsing, S.K., Beniest, A., van der Boon, A., Abels, H.A., Deenen, M.H.L., Ruhl, M., Krijgsman, W., 2014. Astronomically-calibrated magnetostratigraphy of the Lower Jurassic marine successions at St. Audrie's Bay and East Quantoxhead (Hettangian–Sinemurian; Somerset, UK). Palaeogeogr. Palaeoclimatol. Palaeoecol. 403, 43–56.

Huybers, P., 2006. Early Pleistocene glacial cycles and the integrated summer insolation forcing. Science 313, 508–511.

Ikeda, M., Tada, R., Ozaki, K., 2017. Astronomical pacing of the global silica cycle recorded in Mesozoic bedded cherts. Nat. Commun. 8, 15532.

Kent, D.V., Olsen, P.E., 2008. Early Jurassic magnetostratigraphy and paleolatitudes from the Hartford continental rift basin (eastern North America): testing for polarity bias and abrupt polar wander in association with the Central Atlantic magmatic province. J. Geophys. Res. Solid Earth 113.

Kent, D.V., Olsen, P.E., Muttoni, G., 2017. Astrochronostratigraphic polarity time scale (APTS) for the Late Triassic and Early Jurassic from continental sediments and correlation with standard marine stages. Earth Sci. Rev. 166, 153–180.

Kent, D.V., Olsen, P.E., Rasmussen, C., Lepre, C., Mundil, R., Irmis, R.B., Gehrels, G.E., Giesler, D., Geissman, J.W., Parker, W.G., 2018. Empirical evidence for stability of the 405-kiloyear Jupiter-Venus eccentricity cycle over hundreds of millions of years. Proc. Natl. Acad. Sci. USA 115, 6153–6158.

Kodama, K.P., Hinnov, L.A., 2015. Time series analysis for cyclostratigraphy. In: Rock Magnetic Cyclostratigraphy, pp. 52–89.

Korte, C., Ruhl, M., Pálfy, J., Ullmann, C.V., Hesselbo, S.P., 2019. Chemostratigraphy across the Triassic–Jurassic boundary. In: Sial, Alcides N., Gaucher, Claudio, M.R., Ferreira, V.P. (Eds.), Chemostratigraphy Across Major Chronological Boundaries. John Wiley & Sons, pp. 185–210. AGU Books.

Laskar, J., Ogg, James G., Gabi, M., 2020. Astrochronology. In: Gradstein, Felix, Schmitz, Mark D. (Eds.), Geologic Time Scale 2020, pp. 139–158.

Laskar, J., Fienga, A., Gastineau, M., Manche, H., 2011. La2010: a new orbital solution for the long-term motion of the Earth. Astron. Astrophys. 532.

Leu, K., Zeeden, C., Ulfers, A., Abadi, M.S., Vinnepand, M., Ruhl, M., Hesselbo, S.P., Wonik, T., 2024. Astronomical calibration of the Early Jurassic Sinemurian Stage based on cyclostratigraphic studies of downhole logging data in the Prees 2 Borehole (Cheshire Basin, UK). Newsl. Stratigr. 57, 257–282.

Li, M., Huang, C., Hinnov, L., Ogg, J., Chen, Z.-Q., Zhang, Y., 2016. Obliquity-forced climate during the Early Triassic hothouse in China. Geology 44, 623–626.

Li, M.S., Kump, L.R., Hinnov, L.A., Mann, M.E., 2018. Tracking variable sedimentation rates and astronomical forcing in Phanerozoic paleoclimate proxy series with evolutionary correlation coefficients and hypothesis testing. Earth Planet. Sci. Lett. 501, 165–179.

Li, M., Hinnov, L., Kump, L., 2019. Acycle: time-series analysis software for paleoclimate research and education. Comput. Geosci. 127, 12–22.

Liang, L., Sun, Y., Beets, C.J., Prins, M.A., Wu, F., Vandenberghe, J., 2013. Impacts of grain size sorting and chemical weathering on the geochemistry of Jingyuan loess in the northwestern Chinese Loess Plateau. J. Asian Earth Sci. 69, 177–184.

Lodowski, D.G., Martinez, M., P., H.S., Hodbod, M., Leng, M.J., Pieńkowski, G., Brański, P., R., P., 2024. Timing and duration of the early Hettangian marine inundation in the Polish Basin: organic carbon isotopes and astronomical calibration of the Triassic–Jurassic transition of the Niekłań PIG core (Holy Cross Mountains, SE Poland). Vol. Jurass. XXII, 87–116.

Löwemark, L., Bloemsma, M., Croudace, I., Daly, J.S., Edwards, R.J., Francus, P., Galloway, J.M., Gregory, B.R.B., Steven Huang, J.-J., Jones, A.F., Kylander, M., Löwemark, L., Luo, Y., Maclachlan, S., Ohlendorf, C., Patterson, R.T., Pearce, C., Profe, J., Reinhardt, E.G., Stranne, C., Tjallingii, R., Turner, J.N., 2019. Practical guidelines and recent advances in the Itrax XRF core-scanning procedure. Quat. Int. 514, 16–29.

Mann, M.E., Lees, J.M., 1996. Robust estimation of background noise and signal detection in climatic time series. Clim. Chang. 33, 409–445.

Meyers, S.R., 2014. Astrochron: A Computational Tool for Astrochronology. https://cran.r-project.org/package=astrochron.

Meyers, S.R., 2019. Cyclostratigraphy and the problem of astrochronologic testing. Earth Sci. Rev. 190, 190–223.

Page, K.N., 2008. The evolution and geography of Jurassic ammonoids. Proc. Geol. Assoc. 119, 35–57.

Paul, C.R.C., Allison, P.A., Brett, C.E., 2008. The occurrence and preservation of ammonites in the Blue Lias Formation (lower Jurassic) of Devon and Dorset, England and their palaeoecological, sedimentological and diagenetic significance. Palaeogeogr. Palaeoclimatol. Palaeoecol. 270, 258–272.

Percival, L.M.E., Ruhl, M., Hesselbo, S.P., Jenkyns, H.C., Mather, T.A., Whiteside, J.H., 2017. Mercury evidence for pulsed volcanism during the end-Triassic mass extinction. Proc. Natl. Acad. Sci. USA 114, 7929–7934.

Perera, A., Ruhl, M., Xu, W., Silva, R.L., Raine, R., Goodhue, R., 2025. "Short" or "Long" Hettangian? Astronomical chronometry on the duration of lower Jurassic Hettangian stage and the recovery dynamics following the end – Triassic mass extinction. In: EGU General Assembly 2025, Vienna, Austria (pp. EGU25-13954).

Pharaoh, T.C., 1996. Tectonic Map of Britain, Ireland and Adjacent Areas. Sheet 1. 1: 500,000. British Geological Survey, Keyworth, UK.
Plant, J.A., Jones, D.G., Haslam, H.W., Warrington, G., Chadwick, R.A., Milodowski, A. E., Metcalfe, R., Ball, D.F., Bulat, J., Evans, D.J., Gale, I.N., Hooker, P.J., Hyslop, E. K., Jones, N.S., Kemp, S.J., Kirby, G.A., Leng, M.J., Morton, A.C., Nicholson, R.A., Noy, D.J., Rochelle, C.A., Rowley, W.J., Shepherd, T.J., Smith, N.J.P., Spiro, B., Strong, G.E., Walker, A.S.D., Young, S.R., 1999. The Cheshire Basin: Basin Evolution, Fluid Movement and Mineral Resources in a Permo-Triassic Rift Setting. British Geological Survey, Keyworth, Keyworth, Nottingham.
Ruhl, M., Deenen, M.H.L., Abels, H.A., Bonis, N.R., Krijgsman, W., Kürschner, W.M., 2010. Astronomical constraints on the duration of the early Jurassic Hettangian stage and recovery rates following the end-Triassic mass extinction (St Audrie's Bay/ East Quantoxhead, UK). Earth Planet. Sci. Lett. 295, 262–276.
Ruhl, M., Hesselbo, S.P., Hinnov, L., Jenkyns, H.C., Xu, W., Riding, J.B., Storm, M., Minisini, D., Ullmann, C.V., Leng, M.J., 2016. Astronomical constraints on the duration of the Early Jurassic Pliensbachian Stage and global climatic fluctuations. Earth Planet. Sci. Lett. 455, 149–165.
Schaltegger, U., Guex, J., Bartolini, A., Schoene, B., Ovtcharova, M., 2008. Precise U–Pb age constraints for end-Triassic mass extinction, its correlation to volcanism and Hettangian post-extinction recovery. Earth Planet. Sci. Lett. 267, 266–275.
Schoene, B., Guex, J., Bartolini, A., Schaltegger, U., Blackburn, T.J., 2010. Correlating the end-Triassic mass extinction and flood basalt volcanism at the 100 ka level. Geology 38, 387–390.
Scotese, C., 2014. Atlas of Jurassic Paleogeographic Maps, PALEOMAP Atlas for ArcGIS, Volume 4, The Jurassic and Triassic, Maps 32–42, Mollweide Projection, PALEOMAP Project, Evanston, IL.
Sha, J., Olsen, P.E., Pan, Y., Xu, D., Wang, Y., Zhang, X., Yao, X., Vajda, V., 2015. Triassic-Jurassic climate in continental high-latitude Asia was dominated by obliquity-paced variations (Junggar Basin, Urumqi, China). Proc. Natl. Acad. Sci. USA 112, 3624–3629.
Shukri, N., 1942. Rhythmic Bedding in the Lower Lias of England. Faculty of Science Fouad I University Cairo Bulletin, 24, pp. 66–73.
Singh, P., Lu, W., Lu, Z., Jost, A.B., Lau, K., Bachan, A., van de Schootbrugge, B., Payne, J.L., 2023. Reduction in animal abundance and oxygen availability during and after the end-Triassic mass extinction. Geobiology 21, 175–192.
Sinnesael, M., Karatsolis, B.-T., Pearson, P.N., Briais, A., Hemming, S.R., LeVay, L.J., Dunkley Jones, T., Cui, Y., Di Chiara, A., Dodd, J.P., Dwyer, D., Eason, D.E., Friedman, S.A., Hanson, E., Hochmuth, K., Ibrahim, H.E., Jasper, C.E., Lee-Takeda, S., LeBlanc, D.E., Lindsay, M.R., McNamara, D.D., Modestou, S.E., Morris, M.A., Murton, B.J., Oconnell, S., Pasquet, G., Qian, S.-P., Rosenthal, Y., Satolli, S., Suzuki, T., Thulasi, T., Wade, B.S., White, N.J., Wu, T., Yang, A.Y., Parnell-Turner, R.E., 2025. Onset of strong Iceland-Scotland overflow water 3.6 million years ago. Nat. Commun. 16, 4323.
Smith, D.G., 2023. The orbital cycle factory: sixty cyclostratigraphic spectra in need of re-evaluation. Palaeogeogr. Palaeoclimatol. Palaeoecol. 628.
Smith, P.L., Longridge, L.M., Grey, M., Zhang, J., Liang, B., 2014. From near extinction to recovery: Late Triassic to Middle Jurassic ammonoid shell geometry. Lethaia 47, 337–351.
Storm, M.S., Hesselbo, S.P., Jenkyns, H.C., Ruhl, M., Ullmann, C.V., Xu, W., Leng, M.J., Riding, J.B., Gorbanenko, O., 2020. Orbital pacing and secular evolution of the Early Jurassic carbon cycle. Proc. Natl. Acad. Sci. USA 117, 3974–3982.
Thibodeau, A.M., Ritterbush, K., Yager, J.A., West, A.J., Ibarra, Y., Bottjer, D.J., Berelson, W.M., Bergquist, B.A., Corsetti, F.A., 2016. Mercury anomalies and the timing of biotic recovery following the end-Triassic mass extinction. Nat. Commun. 7, 11147.
Tian, J., Wu, H., Huang, C.J., Li, M., Ma, C., 2022. Revisiting the Milankovitch Theory from the Perspective of the 405 ka Long Eccentricity Cycle. Earth Sci. 47 (10), 3543–3568.
Ullmann, C.V., Szücs, D., Jiang, M., Hudson, A.J.L., Hesselbo, S.P., 2021. Geochemistry of macrofossil, bulk rock and secondary calcite in the Early Jurassic strata of the Llanbedr (Mochras Farm) drill core, Cardigan Bay Basin, Wales, UK. J. Geol. Soc. 179.
Ullmann, C.V., Damaschke, M., Hesselbo, S.P., Jiang, M., Lawrence, K., Leng, M.J., Mattioli, E., Bancalin, J., Page, K.N., Pudal, N., Ruhl, M., Silva, R.L., 2026. An integrated biostratigraphy and chemostratigraphy for the dawn of the Jurassic (the Hettangian Stage in the Cheshire Basin, UK). J. Earth Sci. 37, 945–967.
Warrington, G., 1997. The Penarth Group-Lias Group succession (Late Triassic-Early Jurassic) in the East Irish Sea Basin and neighbouring areas: a stratigraphical review. Geol. Soc. Lond. Spec. Publ. 124, 33–46.
Warrington, G., Wilson, A.A., Jones, N.S., Young, S.R., Haslam, H.W., 1999. Stratigraphy and sedimentology. In: Plant, J.A., Jones, D.G., Haslam, H.W. (Eds.), The Cheshire Basin: Basin Evolution, Fluid Movement and Mineral Resources in a Permo-Triassic Rift Setting. The British Geological Survey, Keyworth, p. 263.
Waterhouse, H.K., 1999. Regular terrestrially derived palynofacies cycles in irregular marine sedimentary cycles, Lower Lias, Dorset, UK. J. Geol. Soc. Lond. 156, 1113–1124.
Weedon, G.P., 1986. Hemipelagic Shelf Sedimentation and Climatic Cycles - the Basal Jurassic (Blue Lias) of South Britain. Earth Planet. Sci. Lett. 76, 321–335.
Weedon, G.P., Jenkyns, H.C., 1999. Cyclostratigraphy and the Early Jurassic timescale: data from the Belemnite Marls, Dorset, southern England. Geol. Soc. Am. Bull. 111, 1823–1840.
Weedon, G.P., Jenkyns, H.C., Coe, A.L., Hesselbo, S.P., 1999. Astronomical calibration of the Jurassic time-scale from cyclostratigraphy in British mudrock formations. Philos. Trans. R. Soc. A 357, 1787–1813.
Weedon, G.P., Jenkyns, H.C., Page, K.N., 2017. Combined sea-level and climate controls on limestone formation, hiatuses and ammonite preservation in the Blue Lias Formation, South Britain (uppermost Triassic – Lower Jurassic). Geol. Mag. 155, 1117–1149.
Weedon, G.P., Page, K.N., Jenkyns, H.C., 2019. Cyclostratigraphy, stratigraphic gaps and the duration of the Hettangian Stage (Jurassic): insights from the Blue Lias Formation of southern Britain. Geol. Mag. 156, 1469–1509.
Westerhold, T., Röhl, U., Wilkens, R.H., Gingerich, P.D., Clyde, W.C., Wing, S.L., Bowen, G.J., Kraus, M.J., 2018. Synchronizing early Eocene deep-sea and continental records – cyclostratigraphic age models for the Bighorn Basin Coring Project drill cores. Clim. Past 14, 303–319.
Westerhold, T., Marwan, N., Drury, A.J., Liebrand, D., Agnini, C., Anagnostou, E., Barnet, J.S.K., Bohaty, S.M., De Vleeschouwer, D., Florindo, F., Frederichs, T., Hodell, D.A., Holbourn, A.E., Kroon, D., Lauretano, V., Littler, K., Lourens, L.J., Lyle, M., Palike, H., Rohl, U., Tian, J., Wilkens, R.H., Wilson, P.A., Zachos, J.C., 2020. An astronomically dated record of Earth's climate and its predictability over the last 66 million years. Science 369, 1383–1387.
Whittaker, A., Green, G.W., 1983. Geology of the country around Weston-super-Mare. Memoir of the Geological Survey of Great Britain, Sheet 279, New Series, with parts of sheets 263 and 295., p. 147 pp.
Wotzlaw, J.F., Guex, J., Bartolini, A., Gallet, Y., Krystyn, L., McRoberts, C.A., Taylor, D., Schoene, B., Schaltegger, U., 2014. Towards accurate numerical calibration of the Late Triassic: High-precision U-Pb geochronology constraints on the duration of the Rhaetian. Geology 42, 571–574.
Wu, L., Wilson, D.J., Wang, R., Yin, X., Chen, Z., Xiao, W., Huang, M., 2020. Evaluating Zr/Rb ratio from XRF scanning as an indicator of grain-size variations of glaciomarine sediments in the Southern Ocean. Geochem. Geophys. Geosyst. 21.
Xu, W., Ruhl, M., Hesselbo, S.P., Riding, J.B., Jenkyns, H.C., Petrizzo, M.R., 2016. Orbital pacing of the Early Jurassic carbon cycle, black-shale formation and seabed methane seepage. Sedimentology 64, 127–149. https://onlinelibrary.wiley.com/doi/epdf/10.1111/sed.12329.